

Modeling and Control of a New
Unmanned Aerial Vehicle (SUAVI) with
Tilt-Wing Mechanism

by
Kaan Taha Öner

Submitted to the Graduate School of Sabancı University
in partial fulfillment of the requirements for the degree of
Master of Science

Sabancı University

August, 2009

Modeling and Control of a New Unmanned Aerial Vehicle
(SUAVİ) with Tilt-Wing Mechanism

APPROVED BY:

Assoc. Prof. Dr. Mustafa Ünel
(Thesis Advisor)

.....

Assoc. Prof. Dr. Mahmut Akşit

.....

Assist. Prof. Dr. Kemalettin Erbatur

.....

Assist. Prof. Dr. Hakan Erdoğan

.....

Assist. Prof. Dr. Kayhan Gülez

.....

DATE OF APPROVAL:

.....

© Kaan Taha Öner 2009
All Rights Reserved

Modeling and Control of a New Unmanned Aerial Vehicle (SUAVİ) with Tilt-Wing Mechanism

Kaan Taha Öner

ME, Master's Thesis, 2009

Thesis Supervisor: Assoc. Prof. Mustafa Ünel

Keywords: UAV, Quad-Rotor, Tilt-Wing, Kalman Filter, PID, LQR, IMU

Abstract

Unmanned Aerial Vehicles (UAV) are flying robots that are either controlled by an operator from a remote location or flown autonomously according to the given commands. UAVs are often equipped with cameras, other sensors and communication units and used for missions which are dangerous, tedious or effortful for manned aircrafts. Some applications of these vehicles are surveillance, reconnaissance, traffic monitoring, exploration of disasters (fire, earthquake, flood, etc...) and agricultural pesticide spraying.

This thesis work focuses on the modeling and control of a new quadrotor Unmanned Aerial Vehicle (SUAVİ: Sabancı University Unmanned Aerial Vehicle) with tilt-wing mechanism. The vehicle is capable of vertical take-off and landing (VTOL) like a helicopter and flying horizontally like an airplane. The design specifications and sensor/actuator integration of SUAVİ are presented. A full mathematical model that incorporates the dynamics of horizontal flight, vertical flight and the transition mode is obtained using Newton-Euler formulation. Attitude and position controllers (PID, LQR) are designed in linear framework for the VTOL mode of the vehicle. A controller for transition between vertical and horizontal flight modes is also proposed. All controllers are evaluated in simulations along with 3D visualization. For real-time experiments, Kalman filtering is employed to obtain accurate roll and pitch angle estimations. VTOL experiments with the prototype demonstrate the success of the proposed controllers.

Döner-Kanat Mekanizmalı Yeni bir İnsansız Hava Aracının (SUAVİ) Modellemesi ve Kontrolü

Kaan Taha Öner

ME, Master Tezi, 2009

Tez Danışmanı: Doç. Dr. Mustafa Ünel

Anahtar Kelimeler: İHA, Dört-Rotor, Döner-Kanat, Kalman Filtresi, PID,
LQR, IMU

Özet

İnsansız Hava Araçları (İHA) yer istasyonundaki bir operatör tarafından kontrol edilen ya da verilen komutlara göre otonom olarak uçabilen mobil robotlardır. Kameralar, başka sensörler ve haberleşme sistemleri gibi çeşitli ekipmanlarla donatılan bu araçlar insanlar için tehlike arz eden ya da zorlu görevlerde kullanılmaktadır. Gözetim, keşif, trafik görüntüleme, afet inceleme (yangın, deprem, sel, vb...) ve tarımsal ilaçlama insansız hava araçlarının kullanıldığı çeşitli görevlere örneklerdir.

Bu tez çalışmasında döner kanat mekanizmasına sahip dört rotorlu bir insansız hava aracının (SUAVİ: Sabancı University Unmanned Aerial Vehicle) modellemesi ve kontrolü yer almaktadır. Hava aracı bir helikopter gibi dikey (VTOL) ve bir uçak gibi yatay uçabilecek şekilde tasarlanmıştır. Aracın tasarım özellikleri ve sensör/eyleyici entegrasyonu sunulmuştur. SUAVİ'nin yatay uçuş, dikey uçuş ve iki uçuş modu arasındaki geçiş dinamiklerini içeren matematiksel modeli Newton-Euler metoduyla elde edilmiştir. Aracın VTOL modu için yönelim ve pozisyon kontrolörleri (PID, LQR) tasarlanmıştır. Bir başka kontrolör ise aracın dikey ve yatay uçuş modları arasındaki geçişi sağlamak üzere tasarlanmıştır. Bütün kontrolörler benzetim ortamında incelenmiş ve benzetimler 3 boyutlu olarak görselleştirilmiştir. Gerçek zamanlı deneylerde kullanılmak üzere, Kalman filtresi ile yuvarlanma ve yunuslama açılarının kestirimi yapılmıştır. Prototip ile yapılan VTOL uçuş deneyleri kontrolörlerin başarısını göstermektedir.

Acknowledgements

It is a great pleasure to extend my gratitude to my thesis advisor Assoc. Prof. Dr. Mustafa Ünel for his precious guidance and support. I am greatly indebted to him for his supervision and excellent advises throughout my Master study. I would gratefully thank Assoc. Prof. Dr. Mahmut Akşit, Assist. Prof. Dr. Kemalettin Erbatur, Assist. Prof. Hakan Erdoğan and Assist. Prof. Dr. Kayhan Gülez for their feedbacks and spending their valuable time to serve as my jurors.

I would like to acknowledge the financial support provided by The Scientific & Technological Research Council of Turkey (TÜBİTAK) through the project “Mechanical Design, Prototyping and Flight Control of an Unmanned Autonomous Aerial Vehicle” under the grant 107M179.

I would sincerely like to thank to SUAVİ project members Ertuğrul Çetinsoy, Efe Sırmoğlu, Cevdet Hançer and Taylan Ayken for their pleasant team-work and providing me the necessary motivation during hard times.

Many thanks to Firuze Okyay, Evrim Taşkiran, Yasin Yazıcıoğlu, Utku Seven, Ozan Mutluer, Özer Koca, Metin Yılmaz, Ahmet Can Erdoğan, Berk Çallı, Hakan Ertaş, Eray Baran and all mechatronics laboratory members I wish I had the space to acknowledge in person, for their great friendship throughout my Master study.

Finally, I would like to thank my family for all their love and support throughout my life.

Contents

1	Introduction	1
1.1	Unmanned Aerial Vehicles	1
1.1.1	Micro Aerial Vehicles (MAVs)	2
1.1.2	Small Unmanned Aerial Vehicles (SUAVs)	4
1.1.3	Large Scale Unmanned Aerial Vehicles (UAVs)	4
1.2	Contribution of This Thesis	7
2	The Design of the Aerial Vehicle (SUAVi)	8
2.1	Flying Principles	8
2.1.1	Fixed-Wing Aerial Vehicles	9
2.1.2	Rotary-Wing Aerial Vehicles	10
2.1.3	V/STOL Aerial Vehicles	11
2.2	Aerodynamic Configuration	13
2.2.1	Wing Design	15
2.3	Mechanical Platform	19
2.4	Actuator Integration	21
2.4.1	Rotor & Rotor Driver	21
2.4.2	Propeller	22
2.4.3	Servos	24
2.4.4	Battery	24
2.5	Sensor Integration	26
2.5.1	IMU	26
2.6	Communication	27
3	Kinematic & Dynamic Modeling	28

3.1	Modeling Using Newton-Euler Formulation	29
3.1.1	Coordinate Frames	29
3.1.2	Kinematic Equations	29
3.1.3	Dynamic Equations	31
4	Controller Synthesis	41
4.1	Background	41
4.2	Controller Design in Linear Framework	42
4.2.1	PID Attitude Stabilization	43
4.2.2	PID Position Controller	45
4.2.3	LQR Position Controller	46
4.3	Transition Between Vertical Flight and Horizontal Flight . . .	48
4.4	Attitude Estimation Using Kalman Filtering	49
4.5	Simulations	58
4.5.1	Visualization Using VR Toolbox	58
4.5.2	Simulation Results	61
5	Experimental Results	75
5.1	Kalman Filter Experiments	75
5.2	Vertical Flight Experiments	77
6	Conclusion & Future Works	81

List of Figures

2.1	Aerial vehicle in vertical and horizontal flight modes	14
2.2	Different wing planforms	15
2.3	NACA 2412 Wing profile	16
2.4	Half model in wind tunnel simulation	17
2.5	Streamlines showing the airstream interaction	18
2.6	Stresses appearing on the wing and body under 2.5g acceleration	19
2.7	Universal testing machine	20
2.8	Airframe produced with carbon composite material	20
2.9	Rimfire 42-40-800 kV and Silver Series SS-45	21
2.10	Test rig for thrust measurements	22
2.11	Xoar 14x7 propeller	23
2.12	Current vs. thrust graph of 14x7 propeller (11.1 V)	23
2.13	Tower Hobbies TS-170 digital servo	24
2.14	Li-Po battery	25
2.15	SUAVI with integrated actuators on different flight configura- tions	25
2.16	Sparkfun IMU V4	26
3.1	Coordinate frames of the aerial vehicle	29
3.2	External forces and torques acting on the vehicle	32
3.3	NACA2410 airfoil	33
3.4	Lift vs. Reynolds' number	34
3.5	Effective angle of attack α_i	35
3.6	Lift and Drag coefficients on large angles of attack	35
3.7	Lift force F_L	36
3.8	Drag force F_D	36

3.9	Relationship between thrust and square of angular velocity for 14x7 propeller	37
4.1	Block diagram of the PID controller	45
4.2	Block diagram of cascade PID position controller	46
4.3	Block diagram of the LQR controller	48
4.4	Forces acting during transition	49
4.5	Gyroscope readings around x,y,z axes	51
4.6	Gyroscope readings around x,y,z axes while rotors are running	51
4.7	Accelerometer readings around x,y,z axes	52
4.8	Accelerometer readings around x,y,z axes during hover	53
4.9	Accelerometer readings around x,y,z axes with 10 Hz low pass filter during hover	54
4.10	Accelerometer readings around x,y,z axes with 0.6 Hz low pass filter during hover	54
4.11	Magnetometer readings around x,y,z axes	55
4.12	Roll and pitch angles obtained via integration	56
4.13	Roll and pitch angles obtained with Kalman filters	57
4.14	Simulink model of the SUAVI	58
4.15	Take-Off visualization using VR toolbox	59
4.16	Flight modes visualization using VR toolbox	60
4.17	Attitude control using PID	61
4.18	Forces created by rotors (PID)	62
4.19	Position control using cascade PID	63
4.20	Attitude control using cascade PID	63
4.21	Forces created by rotors (Cascade PID)	64
4.22	Position control using LQR	65

4.23	Attitude control using LQR	66
4.24	Forces created by rotors (LQR)	66
4.25	Rectangle and helix tracking	67
4.26	Rectangle and helix tracking using LQR (position)	67
4.27	Rectangle and helix tracking using LQR (attitude)	68
4.28	Rectangle and helix tracking using LQR (rotor forces)	68
4.29	Position control (LQR)	69
4.30	Attitude control (LQR)	70
4.31	Forces created by rotors (LQR)	71
4.32	Change of tilt angles	72
4.33	Airstream magnitude and its angle during transition	72
4.34	Effective angle of attack during transition	73
4.35	Lift and drag forces during transition	73
4.36	Rotor forces during transition	74
4.37	Altitude regulation during transition	74
5.1	SUAVÍ prototype and the quadrotor test platform	75
5.2	Roll estimation using Kalman filter (static)	76
5.3	Pitch estimation using Kalman filter (static)	76
5.4	Roll estimation using Kalman filter (dynamic)	77
5.5	Pitch estimation using Kalman filter (dynamic)	77
5.6	Attitude stabilization experiment using PID	78
5.7	Attitude stabilization experiment using PID	79
5.8	Attitude stabilization experiment using PID	79
5.9	SUAVÍ vertical flight experiment	80

List of Tables

1.1	Some MAV projects and specifications	3
1.2	Some SUAV projects and specifications	5
1.3	Some UAV projects and specifications	6
2.1	Flying principles comparison (1=bad, 5=good)	9
2.2	Rotary-Wing configurations compared (1=bad, 4=good) . . .	10
2.3	Tilt-Rotor & Tilt-Wing aerial vehicles history	12
2.4	Current Tilt-Wing & Tilt-Rotor SUAV projects	13
2.5	Tensile strength test of carbon composite material	20
2.6	Propeller current draw on max. static thrust test	22
4.1	Position control & attitude stabilization performances	70

Chapter I

1 Introduction

Mobile robots with autonomous control capabilities have always been a fascinating subject among researchers. It has been more than 20 years that an autonomous land vehicle has performed road tracking with computer vision algorithms for the first time in 1988 [1]. Since then many autonomous mobile robots that work on land, water and air have been developed for industrial, civil and military use. Even though aerial vehicles offered a broader field of applications they remained unreachable because of their high costs for a long time. In the last decade with the advances in sensor, actuator and power technologies these vehicles turned into affordable platforms for researches and a new trend has started.

1.1 Unmanned Aerial Vehicles

An Unmanned Aerial Vehicle (UAV) (or sometimes referred as an Unmanned Aircraft System) is a mobile robot that is either controlled from a ground station or flown autonomously with high level control algorithms. UAVs are often equipped with cameras, sensors and communication units and used for missions which are dangerous tedious or effortful for manned aircraft. There are a plenty number of commercial and non-commercial UAVs with different shapes, sizes and configurations. These variety of designs come

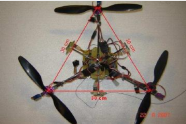





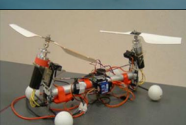


from the wide range of the missions and objectives they are used for. In today's world many people have heard of UAVs from the military drones which are used for reconnaissance and attack missions. However traffic monitoring, exploration of disasters (fire, earthquake, flood, etc...) and agricultural pesticide spraying are civilian examples of use for these vehicles.

According to a market investigation held in 2009 [2], 22 industrial and twice as much research groups are currently working on UAVs. A total number of 6695 UAVs are reported to be operating in NATO nations [3] and 294 different UAV models for civil and commercial applications are referenced in [4]. A global consensus of classification method for these UAVs is not established yet, nevermore these vehicles can be investigated under three main categories:

1.1.1 Micro Aerial Vehicles (MAVs)

Although the aerial vehicles that fit in this category are limited to a size less than 15 cm by DARPA's (Defense Advanced Research Projects Agency) 1997 definition [5], fixed-wing planes, helicopters, ducted fans, blimps and some other bird/insect like flying platforms that have a wingspan of no more than 50 cm or weigh less than 1 kg's are referred as MAVs today. The applications of these vehicles are mainly aerial exploration and surveillance under altitudes of 100 meters however high altitude MAVs also exist. Generally they are equipped with MEMS sensors, powered by Li-Po batteries and actuated with DC electric motors/rotors. Table 1.1 summarizes some existing MAV projects [6]-[14].

Table 1.1: Some MAV projects and specifications

Project Name		Width [cm]	Length [cm]	Weight [kg]	Payload [kg]	Range [km]	Endurance [min]	Max Speed [km/h]	Hover?
Delta of UTC [6]		30	30	0.45	0.2	N/A	N/A	N/A	Yes
MAV of Drexel [7]		76	N/A	0.6	0.4	N/A	N/A	N/A	Yes
Black Widow of AeroVironment [8]		15	15	0.08	N/A	1.8	30	48	No
Delfly Micro of Delft [9]		10	10	0.003	N/A	0.05	3	N/A	No
Ornithopter of Utah [10]		60	N/A	0.097	N/A	N/A	9-10	N/A	No
Blimp II of EPFL [11]		110	60	0.1	0.2	Indoor	120-180	3.6	Yes
Birotor of Compiègne [12]		20	20	1	N/A	N/A	N/A	N/A	Yes
Draganflyer X6 of DraganFly [13]		91	85	1	0.5	2.4	20	50	Yes
T-Hawk of Honeywell [14]		33	33	7.7	N/A	10	50	74	Yes

1.1.2 Small Unmanned Aerial Vehicles (SUAVs)

SUAVs (or sometimes called Mini UAVs) are generally interpreted to be packable and portable aircrafts that can be carried from one location to another by a single human operator. Their dimensions are at most 3 m in width or length [15] which are mostly well known fixed wing planes or helicopters. A great percentage of existing aerial vehicles are in SUAV segment and these vehicle have started being substituted instead of their much more expensive large scales. That is because the SUAVs cost several thousand dollars whereas the large scale UAVs cost up to several million dollars. For example, U. S. Army have been using the Raven RQ-11B from AeroVironment in surveillance missions of Iraq war [16]. Some important examples to these segment of aerial vehicles are given in Table 1.2 with their specifications [17]-[24].

1.1.3 Large Scale Unmanned Aerial Vehicles (UAVs)

The aerial vehicles that fit in this category are designed for endurance, range or large payload capability and they go up to scales of airliner planes. With the budgets going up to 40 million \$ these aerial vehicles are mainly in the hands of professional aircraft manufacturers. Only the Yamaha R-Max (the smallest one) from this class, is known to be used for research purposes and civil applications. Table 1.3 summarizes some important examples to this class of UAVs [25]-[30].

Table 1.2: Some SUAV projects and specifications

Project Name		Width [m]	Length [m]	Weight [kg]	Payload [kg]	Range [km]	Endurance [min]	Max Speed [km/h]	Hover?
Raven of AeroVironment [17]		1.4	0.9	1.9	0.2	10	60-90	81	No
Desert Hawk of Lockheed Martin [18]		1.37	0.91	3	1	15	90	N/A	No
Orbiter of AAI Corp. [19]		2.2	0.91	6.5	N/A	45	120-180	139	No
Malazgirt of Baykar Tech. [20]		1.8	1.2	12	1	20	35/90 ¹	N/A	Yes
QTW UAS F4 of GH Craft [21]		1.8	1.86	30	5	20	60	150	Yes
Tango of DraganFly [22]		1.5	1.2	2.8	1.14	N/A	50	95	No
Blimp 2C of Survey Copter [23]		1.2	3	N/A	0.9	N/A	60	N/A	Yes
Tailsitter of Brigham [24]		1	0.65	1.37	0.2	N/A	2.5/15 ²	54	Yes

¹electric/gasoline

²hover/level flight

Table 1.3: Some UAV projects and specifications

Project Name		Width [m]	Length [m]	Weight [kg]	Payload [kg]	Range [km]	Endurance [h]	Max Speed [km/h]	Hover?
R-Max of Yamaha [25]		2	3.63	95	N/A	2	1.5	20	Yes
Fire Scout of Northrop Grumman [26]		9.2	8.4	1428	300	200	6.1	231	Yes
Eagle Eye of Bell Helicopter [27]		7.3	5.5	N/A	91	N/A	6	360	Yes
Predator of General Atomics [28]		17	8	1043	204	730	40	222	No
Global Hawk of Northrop Grumman [29]		39.9	14.5	14628	1360	N/A	35	574	No
Helios of NASA [30]		75.3	2.44	1052	N/A	N/A	30	N/A	No

1.2 Contribution of This Thesis

- A mathematical model of a new quadrotor unmanned aerial vehicle with tilt-wing mechanism (SUAVİ: Sabancı University Unmanned Aerial Vehicle) that incorporates the flight dynamics of horizontal flight, vertical flight and transition process is obtained using Newton-Euler formulation. SUAVİ is being developed in the context of a TÜBİTAK (The Scientific & Technological Research Council of Turkey) funded research project under the grant 107M179.
- Position controller and attitude stabilizer are designed in linear framework for vertical flight and a method for transition process is presented.
- Robust roll and pitch angle estimations are obtained for attitude stabilization with Kalman filtering using low-cost MEMS sensors employed in IMU. The performance of the filters in high frequency vibration environment are verified with flight experiments.
- A flight simulator with joystick input and 3D visualization toolbox is developed in Simulink/Matlab environment.
- Several vertical flight experiments have been performed in real time approximately for 50 sec. in hovering conditions.

Chapter II

2 The Design of the Aerial Vehicle (SUAVİ)

The design motivation of the aerial vehicle (SUAVİ¹) is shaped considering the missions it will carry out. For observation of indoor and outdoor spaces of large buildings and storages a MAV or SUAV scale electrically actuated platform is chosen as the vehicle class. Twenty five minutes hover and ninety minutes level flight are set as desired endurance characteristics for a successful monitoring and exploration of disasters like fire, earthquake, flood and other events. To start with the design procedure, the physical characteristics of the aerial vehicle are defined as follows:

- a maximum width/length of 1 m
- a maximum weight of 4 kg
- VTOL (Vertical Take-Off and Landing) configuration
- 40-70 km/h horizontal flight speed

2.1 Flying Principles

In the design process of an aerial vehicle, many flying concepts need to be explored for success. Including the self lifting vehicles, the flying principles

¹SUAVİ is being developed in the context of a TÜBİTAK (The Scientific & Technological Research Council of Turkey) funded research project under the grant 107M179.

of aerial vehicles can be investigated under four main categories; Fixed-Wing Aerial Vehicles, Rotary-Wing Aerial Vehicles, Blimps and V/STOL (Vertical Short Take-Off and Landing) Vehicles that combine Fixed-Wing and Rotary-Wing flying concepts. Table 2.1 adapted from [31] gives a comparison of these flying concepts for the MAV and SUAV class vehicles.

Table 2.1: Flying principles comparison (1=bad, 5=good)

	Fixed-Wing	Rotary-Wing	Blimp	V/STOL
Power Cost	3	1	5	2
Control Effort	3	1	5	1
Payload/Volume	5	3	1	4
Manoeuvrability	3	5	1	5
Stationary Flight	1	5	5	5
Low Speed Flight	1	5	5	5
High Speed Flight	5	3	1	4
Hover	1	5	5	5
Endurance	4	1	5	3
Miniaturization	3	5	1	3
Indoor Use	1	5	3	4
Total	30	39	37	41

From this comparison one can see that V/STOL Vehicles that combine Fixed-Wing and Rotary-Wing structures together have the most promising mission performance for the MAV/SUAV class platforms.

2.1.1 Fixed-Wing Aerial Vehicles

For missions that demand endurance and long flight range, fixed-wing type aerial vehicles are preferred to rotary-wing vehicles. To remain at a

constant altitude a fixed-wing vehicle’s energy consumption is considerably small compared to a rotary-wing vehicle that has to put a lot its effort to compensate for gravity. This flying principle is often used in SUAV and UAV class to achieve robust and stable flight. Although near target surveillance and hovering is not achievable with a fixed-wing aerial vehicle, some wing configurations allow as low as 30-40 km/h airspeeds.

2.1.2 Rotary-Wing Aerial Vehicles

Rotary-Wing vehicles are capable of Vertical Take Off/Landing (VTOL) which is a great advantage for many applications. The hovering ability and very low flight speed makes them good candidates for MAV and SUAV applications like target tracking and indoor use. A comparison of Rotary-Wing configurations adapted from [31] is given in Table 2.2.

Table 2.2: Rotary-Wing configurations compared (1=bad, 4=good)

	<i>Single Rotor</i>	<i>Axial Rotor</i>	<i>Coaxial Rotors</i>	<i>Tandem Rotors</i>	<i>Quadrotor</i>
Power Cost	2	2	2	2	1
Control Effort	1	1	4	2	3
Payload/Volume	2	2	4	3	3
Manoeuvrability	4	3	2	2	3
Stationary Flight	4	4	4	4	4
Low Speed Flight	4	3	4	3	4
High Speed Flight	2	4	1	2	3
Miniaturization	2	3	4	2	4
Total	21	22	25	20	25




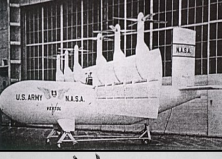





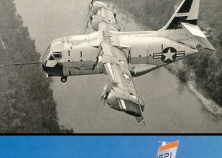




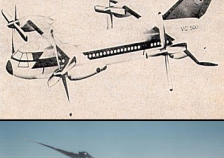



From the Table 2.2, one can see that the Quadrotor and Coaxial-Rotors are more advantageous on an overall evaluation and therefore they may be preferred over other rotary-wing configurations in MAV/SUAV applications.

2.1.3 V/STOL Aerial Vehicles

This class of aircraft uses a single propulsion system that alters the direction of thrust for hover or cruise, or alters the attitude of the aircraft itself [32]. The V/STOL Aerial Vehicle configurations can be summarized under three main principles: Tilt-Rotor, Tilt-Wing and Tailsitter vehicles.

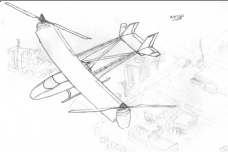




The Tailsitters are fixed wing airplanes that can take off above their tails like a rocket using the thrust of the propeller. These vehicles are not suitable for hovering type missions and the vertical flight is only limited to take off and landing process. The Tilt-Rotor and Tilt-Wing aerial vehicles however combine the advantages of horizontal and vertical flight. They are in general hard to fly vehicles which require advanced control and actuation technologies for a safe flight. Tilting the entire wing, instead of just the rotor or propeller, provides the benefit of increasing aerodynamic flow over the lifting and control surfaces during transition, and minimizes the lift loss due to downwash in hover [32]. Considering that the number of rotors is affecting the controllability and the stability of the aerial vehicle directly, the general attitude on these vehicle's rotor configurations is to have two or four symmetrically placed rotors, which can be rotated from vertical to horizontal position, as can be seen from the chronological guide of existing vehicles given in Table 2.3 [33].

Table 2.3: Tilt-Rotor & Tilt-Wing aerial vehicles history

Project Name	Year	Project Name	Year
1-G of Transcendental	 1954	XV-3 of Bell	 1955
VZ-2 of Vertol	 1955	Tilt-Wing of Vertol-NASA	 1959
VZ-4 of Doak	 1958	X-18 of Hiller	 1959
K-16 of Kaman	 1962	X-100 of Curtis Wright	 1960
X-100 of Curtis Wright	 1964	XC-142 of LTV-Hiller-Ryan	 1964
CL-84 “Dynavert” of Canadair	 1965	X-22 of Bell	 1966
Nord 500 of Nord Aviation	 1968	VC-400 of VFW	 1969
VC-500 of VFW	 N/A	XV-15 of Bell	 1980
V-22 “Osprey” of Bell-Boing	 1989	BA-609 of Bell-Agusta	 1999

Until 2000's the Tilt-Wing and Tilt-Rotor flying concepts remained only applied to manned aircrafts. UAVs capable of both horizontal and vertical flight are newly being explored. The current Tilt-Rotor and Tilt-Wing research is summarized in Table 2.4.

Table 2.4: Current Tilt-Wing & Tilt-Rotor SUAV projects

Institute		Project	Configuration	Year
Florida Institute of Technology		VERTIGO	Tilt-Rotor	2004-?
Arizona State University		HARVee	Tilt-Wing	2004-?
Korea Aerospace Research Institute		Smart UAV	Tilt-Rotor	2004-2009
Chiba University & G.H. Craft		QTW UAS-FS4	Tilt-Wing	2006-2009
AVT		Hammerhead	Tilt-Rotor	2003-2009

2.2 Aerodynamic Configuration

The aerodynamic design stage of the vehicle is a crucial part of the development phase, because it also puts constraints on the mechanical design of the vehicle. For good hovering properties and vertical flight performance the

Rotary-Wing flying configuration is determined to be the quadrotor type. As explained in Chapter I, this configuration has been adapted to various V/STOL platforms and has the advantages of mechanical simplicity and large payload capacity compared to other Rotary-Wing platforms. In order to realize the symmetrical structure of a quadrotor with minimum actuation complexity, the vehicle is designed with four equal wings that are mounted on the front and at the back of the vehicle. The Tilt-Wing configuration is chosen instead of a Tilt-Rotor in order to minimize the downwash effects. To obtain the maximum volume for placing the electronic equipment, a rectangular cross-sectioned body with the shape of a symmetric wing profile is selected as the fuselage. With this wing and body configuration, the vehicle's airframe transforms into a quadrotor structure if the wings are at the vertical position and into a tandem wing airplane structure if the wings are at the horizontal position Fig. 2.1.

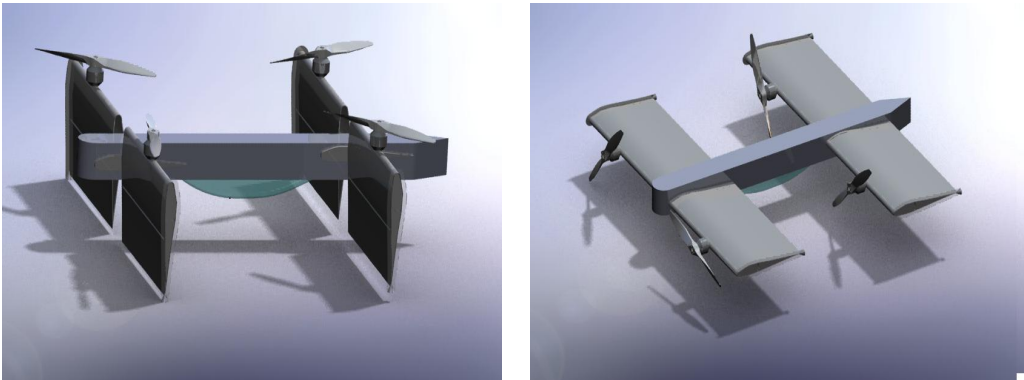


Figure 2.1: Aerial vehicle in vertical and horizontal flight modes

To keep the control complexity in horizontal flight mode on a minimum level, the rotations of the wings are used as attitude control inputs in addition to motor thrust inputs of the vehicle. Therefore using additional control

surfaces that are put on trailing edges of the wings on a regular airplane are eliminated. The two wings on the front are designed to be rotated independently whereas the two wings at the back are designed to be rotated together. This way the control surfaces of a regular plane in horizontal flight mode are mimicked with minimum number of actuators. To achieve this type of a flight control structure a precise wing design and analysis need to be performed which includes the selection of a wing profile, determination of the physical dimensions and the analysis of the airstream interactions between the wings.

2.2.1 Wing Design

Different wing planforms (2D projections) with stall progression patterns are shown in Fig. 2.2 [34].

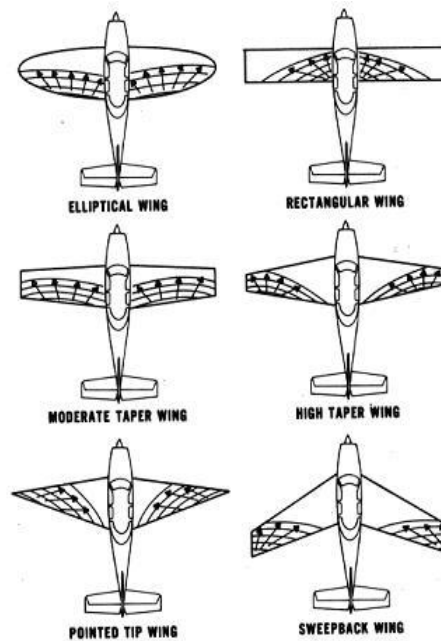


Figure 2.2: Different wing planforms

Compared to other shapes the rectangular planform has some advantages of simplicity as explained in [34]:

“In comparison, the rectangular wing has a tendency to stall first at the wing root and provides adequate stall warning, adequate aileron effectiveness, and is usually quite stable. It is, therefore, favored in the design of low cost, low speed airplanes.”

“Note that it is possible for the trailing edge of the inboard portion of the rectangular wing to be stalled while the rest of the wing is developing lift. This is a very desirable characteristic, and along with simplicity of construction is the reason why this type of wing is so popular in light airplanes, despite certain structural and aerodynamic inefficiencies.”

To start with, NACA2412 , a well known wing profile in the literature, with rectangular wing planform is chosen as the wing profile for the vehicle. Using JavaFoil[®] software, coordinates of 60 sample points from the wing profile are obtained for CAD modeling (Fig. 2.3).

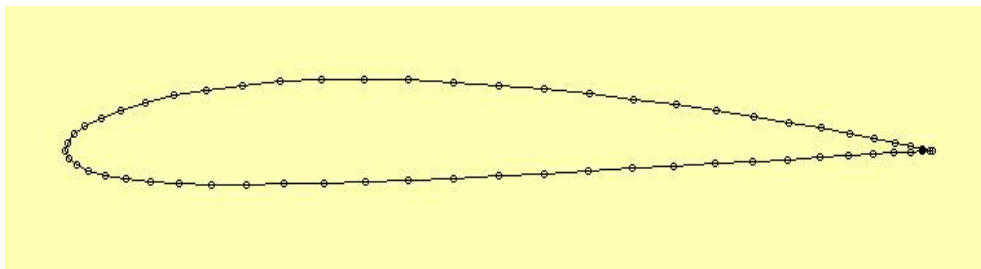


Figure 2.3: NACA 2412 Wing profile

After modeling the airframe of SUAVİ the CAD model is imported to

ANSYS® for CFD analysis (Fig. 2.4). A wind tunnel simulation environment is created with proper inlet, outlet, body and propeller boundary conditions.

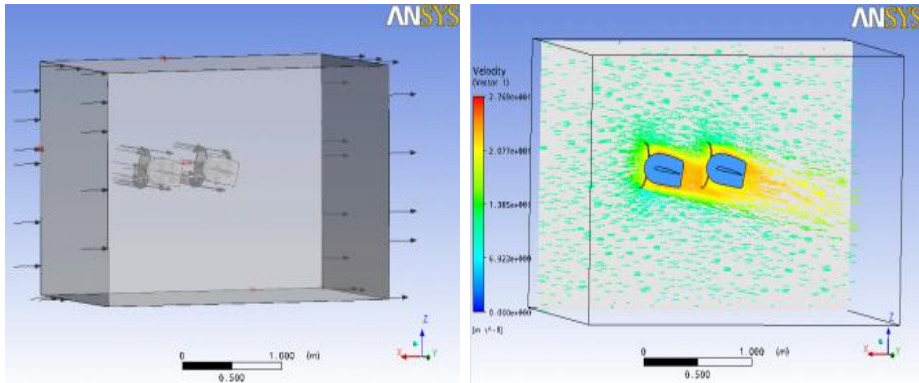


Figure 2.4: Half model in wind tunnel simulation

Simulations done by ANSYS® showed that the NACA2412 wing profile with 25 cm chord length and 45 cm span produced more than 10 N lift thrust that has to be generated by each of four wings on aimed flight speeds (40-70 km/h). To reduce the drag forces further, the wing profile is replaced with NACA2410 which consists of a 2% smaller camber. Simulations repeated with NACA2410 wing profile with the same chord and span dimensions showed that the desired lift forces (10 N per Wing) are obtained with a minor improvement on drag forces. A first draft of the aerodynamic design appears in [35].

Airstream Interaction Between Front and Rear Wings

The difference between the angle of attacks of the wings on the front and at the back of the vehicle is a result of change in the airstream caused by the front wing .

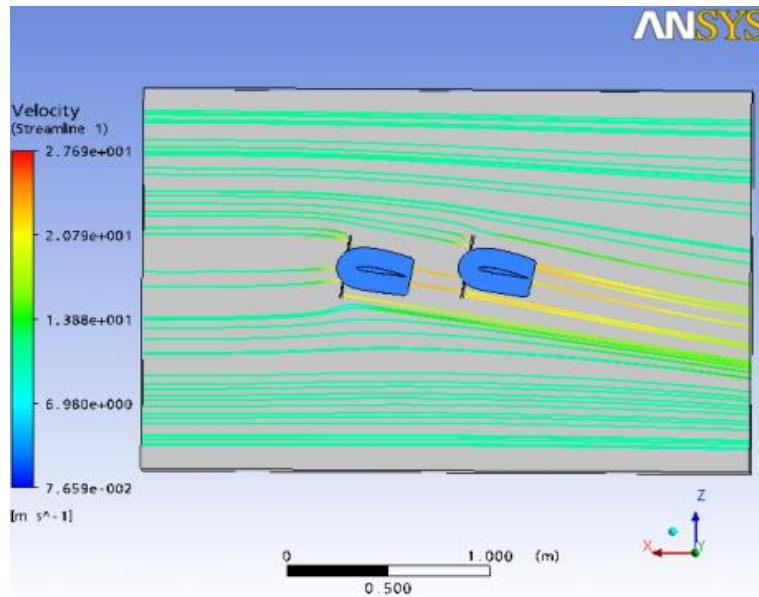


Figure 2.5: Streamlines showing the airstream interaction

To minimize the interaction of the wings, it is suggested to put the wings at the back of the vehicle on a different height level such that the airstreams of the wings on the front will not interact with the wings at the back. However, simulations showed that the height difference, needed to overcome these interactions, is a large distance compared to the size of the aerial vehicle (as can be seen from the streamlines in Fig. 2.5), so the wings are left on the same height level. With this wing configuration at a flight speed of 40 km/h, the angle of attacks needed to achieve necessary lift forces are obtained as 10.5° for the wings on the front and 12.5° for the wings at the back of the vehicle. For a flight speed of 68 km/h these angle of attacks are computed as 2° for the wings on the front and 3.7° for the wings at the back of the vehicle.

2.3 Mechanical Platform

The main motivation behind the mechanical design is to construct a very light weight structure that can withstand to loading forces that occur during vertical and horizontal flight. To achieve this goal, the material of the vehicle is chosen to be carbon composite with sandwich structure that has better compression and tension properties compared to layered carbon structures. The FEM analysis made in ANSYS® showed that under an acceleration of 2.5 g, the maximum stress that appears on the airframe has a magnitude of 4 MPa. The location of this stress point is on the bottom of the body where the 2.4 kg heavy batteries will be placed (Fig. 2.6).

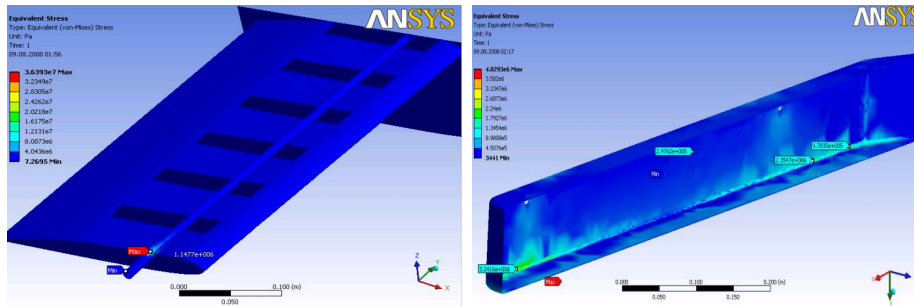


Figure 2.6: Stresses appearing on the wing and body under 2.5g acceleration

Tensile Strength Test

Using the “Universal Testing Machine” (Fig. 2.7) 25x250 mm sized composite carbon sandwich structures with 6 mm² cross section are tested for tensile strength using 2 mm/min separation speed. From different samples a mean value of 27 GPa tensile strength is obtained for the carbon composite material (Table 2.5), thus the material can withstand the predicted stresses and is therefore suitable for the airframe. Fig. 2.8 shows the airframe of the

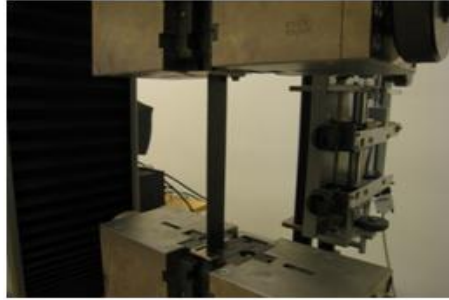


Figure 2.7: Universal testing machine

vehicle produced with this carbon sandwich structure.

Table 2.5: Tensile strength test of carbon composite material

L_c mm	F(0.2 %) N	F(0.3 %) N	EM2 MPa	S_0 mm ²	F(0.1 %) N	F(0.2 %) N	Gradient MPa	F_{max} MPa	Strain F_{max} %	F at Break N	Strain Break %
100	419.43	542.59	20525	6.00	255.41	419.43	27337	524.72	2.78	3029	2.78
100	455.04	582.02	21162	6.00	285.69	455.04	28225	541.88	2.64	3186	2.65
100	410.27	535.20	20821	6.00	248.39	410.27	26981	560.01	2.82	3286	2.82
100	392.40	541.21	24801	6.00	220.60	392.40	28632	506.39	2.54	3038	2.54



Figure 2.8: Airframe produced with carbon composite material

2.4 Actuator Integration

The actuation system of SUAVI consists of rotors, rotor drivers, propellers, servos and batteries.

2.4.1 Rotor & Rotor Driver

For a 4 kg aerial vehicle with hovering capabilities, the minimum thrust to be generated is determined as 6 kg which is composed of 1 kg nominal thrust, 0.25 kg control margin and 0.25 kg payload capacity for each rotor. After some investigation of different rotor types, Great Planes Rimfire 42-40-800kV outrunner brushless rotors (Fig. 2.9) are chosen as the actuators of the vehicle. This high torque, light weight (148 g) rotors are providing a maximum of 592 Watt constant power with 32 A current on input voltages of 11.1 V - 18.5 V [36].



Figure 2.9: Rimfire 42-40-800 kV and Silver Series SS-45

Silver Series SS-45 are chosen as electronic speed controllers (ESC) to drive the Rimfire rotors as suggested by the rotor specifications. The 48 g weighing driver can supply up to 45 A constant current and provide 500 Watt operation power at a control frequency of 50 Hz [37].

2.4.2 Propeller

Different propellers with standard sizes 11x8, 12x8, 13x6.5, 13x8, 14x7 and 14x8.5 of APC are tested on the Rimfire 42-40-800kV rotor in laboratory environment to find the best combination of the components. A test rig with a force gauge has been built (Fig. 2.10) and the propellers are tested under two different voltage levels (11.1 V and 14.8 V) for maximum static thrust and efficiency.



Figure 2.10: Test rig for thrust measurements

The results of maximum static thrust test are given in the table below:

Table 2.6: Propeller current draw on max. static thrust test

Size	11.1 V			14.8 V		
	Current [A]	Max. Thrust [kg]	Thrust/Current [kg/A]	Current [A]	Max. Thrust [kg]	Thrust/Current [kg/A]
11x8	19.1	1.06	0.056	30.2	1.73	0.057
12x8	21.7	1.25	0.058	34.6	2.02	0.058
13x6.5	23.4	1.50	0.064	36.2	2.25	0.062
13x8	24.7	1.47	0.059	39	2.33	0.059
14x7	27.6	1.73	0.063	41.1	2.49	0.061
14x8.5	30.8	1.76	0.057	41.9	2.35	0.056

13x6.5 and 14x7 have been found to be the most efficient propeller sizes

on both operating voltage levels. Because the desired thrust values can be generated on 11.1 V, this voltage level has been chosen as the operating voltage level of the actuators. To come up with a conclusive result the efficiency tests are repeated around nominal thrust (1 kg) value. Within this test 14x7 propeller has performed a slightly better current/thrust ratio and this propeller size is chosen for the actuation system (Fig. 2.11).



Figure 2.11: Xoar 14x7 propeller

The obtained thrust and current relationship for the 14x7 sized propeller is given in Fig. 2.12.

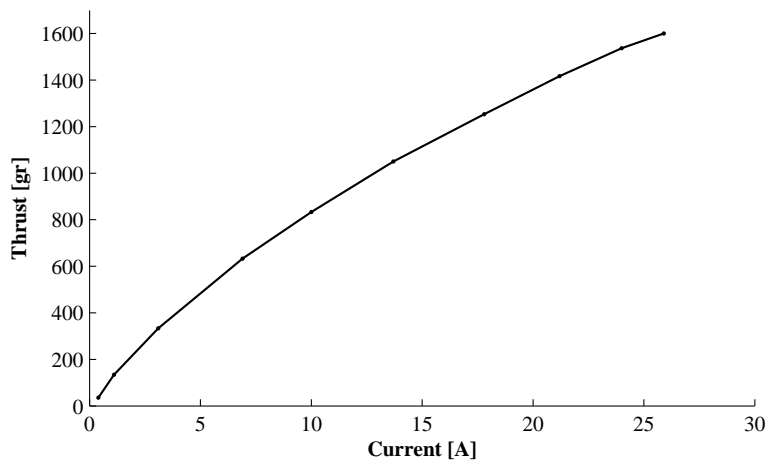


Figure 2.12: Current vs. thrust graph of 14x7 propeller (11.1 V)

2.4.3 Servos

Tower Hobbies TS-170 digital servos are used in the tilt mechanism of the vehicle. These high torque servos have a maximum 1.77 Nm output torque at 4.8 V operating voltage level. Fig. 2.13 shows the TS-170 digital servo.



Figure 2.13: Tower Hobbies TS-170 digital servo

2.4.4 Battery

In order to get on the 11.1 V operating voltage level, three 3.7 V Li-Po cells (Fig. 2.14) with 2400 mAH energy storage capacity are connected in series for each of the rotors.



Figure 2.14: Li-Po battery

Although high energy capacity and light weight Li-Po batteries are used as the power source of actuation, batteries still consist the greatest percentage of the aerial vehicle's weight. Each battery cell has a weight of 160 g and a total

number of 12 battery cells consist a 1.92 kg total weight. Fig. 2.15 shows the SUAVI prototype with integrated actuators on different flight configurations.

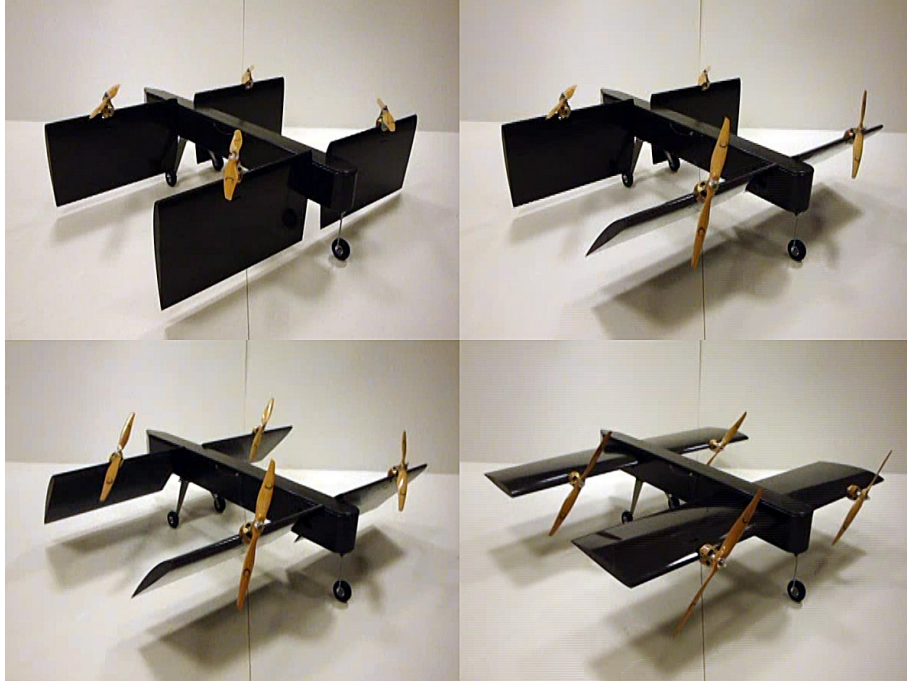


Figure 2.15: SUAVI with integrated actuators on different flight configurations

2.5 Sensor Integration

2.5.1 IMU

For stabilization, control and attitude estimation purposes, SUAVI is equipped with Sparkfun V4 Inertial Measurement Unit (IMU) that consists of 3 axis gyroscopes from InvenSense, 3 axis accelerometers from FreeScale and 3 axis magnetometers from Honeywell (Fig. 2.16).

Control of the Sparkfun IMU is provided through a LPC2138 ARM7 processor. Sensor readings are available with 10 Bit precision from this processor

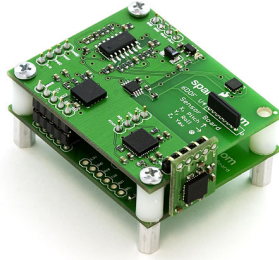


Figure 2.16: Sparkfun IMU V4

over TTL communication at 115200 kbps [38]. Custom filters and sensor fusion algorithms are implementable inside this controller such that the Euler angles defining the attitude of the vehicle with reference to the ground are output instead of raw sensor readings. In order to implement such an algorithm each sensor components characteristics are explored in Chapter IV. The sensor and actuator integration presented in this chapter will appear in [39].

2.6 Communication

Communication between the ground station and SUAV \dot{I} is established via an Futaba RC Transmitter and a Roving Networks Bluetooth module. The RC Transmitter is used to send operator commands to the vehicle whereas the Bluetooth connection is used for monitoring purposes.

Chapter III

3 Kinematic & Dynamic Modeling

The kinematic and dynamic modeling of a Quad Tilt Wing aerial vehicle is a challenging engineering problem. Many well known mathematical models have been developed for fixed wing airplanes [40], quadrotors [41, 42, 43, 44, 31] and tilt-rotor vehicles with two rotors [45, 46, 47]. A mathematical model for the Quad Tilt Wing configuration on a SUAV class vehicle (Low Reynolds' Number) is not developed yet, whereas a dynamic model via identification methods have been established by Nonami *et al.* [48].

SUAVI's full dynamic model consists of horizontal flight using aerodynamic lift of the wings, vertical flight using thrust of the rotors and the transition process that incorporates both horizontal and vertical flight dynamics. Newton-Euler formulation is used to obtain a unified Quad Tilt Wing dynamic model while following assumptions are made:

- The center of mass and the body fixed frame origin are coincident.
- The structure is rigid.
- The drag force of the fuselage is neglected.
- The relative airspeed on the body frame is only due to vehicle's flight speed.

3.1 Modeling Using Newton-Euler Formulation

The dynamic model of the aerial vehicle is developed under the light of the works presented in [31, 44, 45]. A first draft of the dynamic model appears in [49],[50].

3.1.1 Coordinate Frames

Two reference frames are defined for kinematic modeling of the aerial vehicle:

- body fixed reference frame $B : (O_b, x_b, y_b, z_b)$
- earth fixed inertial reference frame $W : (O_w, x_w, y_w, z_w)$.

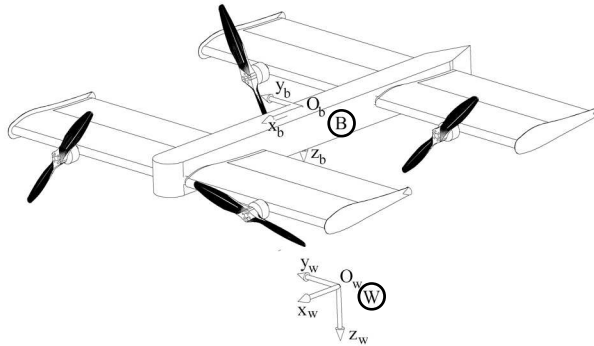


Figure 3.1: Coordinate frames of the aerial vehicle

3.1.2 Kinematic Equations

For the given coordinate frames, the equations describing the position and attitude of the vehicle are obtained by 6 DOF kinematic equations. The

position and linear velocity of the vehicle's center of mass in world frame W are described as,

$$P_w = \begin{bmatrix} X \\ Y \\ Z \end{bmatrix}, V_w = \dot{P}_w = \begin{bmatrix} \dot{X} \\ \dot{Y} \\ \dot{Z} \end{bmatrix}$$

The attitude and angular velocity of the vehicle in world frame W are described as,

$$\alpha_w = \begin{bmatrix} \phi \\ \theta \\ \psi \end{bmatrix}, \Omega_w = \dot{\alpha}_w = \begin{bmatrix} \dot{\phi} \\ \dot{\theta} \\ \dot{\psi} \end{bmatrix}$$

where, ϕ , θ , ψ are named roll, pitch and yaw angles respectively. The equations for the transformation of the angular and linear velocities between world frame W and body frame B are given in equations (1) and (2):

$$V_b = \begin{bmatrix} v_x \\ v_y \\ v_z \end{bmatrix} = R(\phi, \theta, \psi) \cdot V_w \quad (1)$$

where

$$R(\phi, \theta, \psi) = R_z(\psi)R_y(\theta)R_x(\phi)$$

and

$$\Omega_b = \begin{bmatrix} p \\ q \\ r \end{bmatrix} = E(\phi, \theta) \cdot \Omega_w \quad (2)$$

where

$$E(\phi, \theta) = \begin{bmatrix} 1 & 0 & -s_\theta \\ 0 & c_\phi & s_\phi c_\theta \\ 0 & -s_\phi & c_\phi c_\theta \end{bmatrix}$$

The transformation matrix $E(\phi, \theta)$ is obtained from the relationship $\dot{R} = S(\omega_b)R$ where $S(\omega_b)$ is a skew-symmetric matrix [51]. The abbreviations s_β and c_β are used instead of $\sin(\beta)$ and $\cos(\beta)$ respectively.

3.1.3 Dynamic Equations

The dynamic equations obtained for 6 DOF rigid body transformation of the aerial vehicle in body fixed reference frame B are given as:

$$F_t = m\dot{V}_b + \Omega_b \times (m \cdot V_b) \quad (3)$$

$$M_t = I_b\dot{\Omega}_b + \Omega_b \times (I_b \cdot \Omega_b) \quad (4)$$

where m is the mass and the I_b is the inertia matrix expressed in the body frame B . The external forces and torques acting on the vehicle are given in Fig.3.2.

The 6 DOF dynamic equations (3) and (4) describing the rigid body motion are valid for horizontal flight, vertical flight and for transition process. However the external forces F_t and external moments M_t are functions of the tilt angle θ_{1-4} and show very different actuation dynamics for different flight modes.

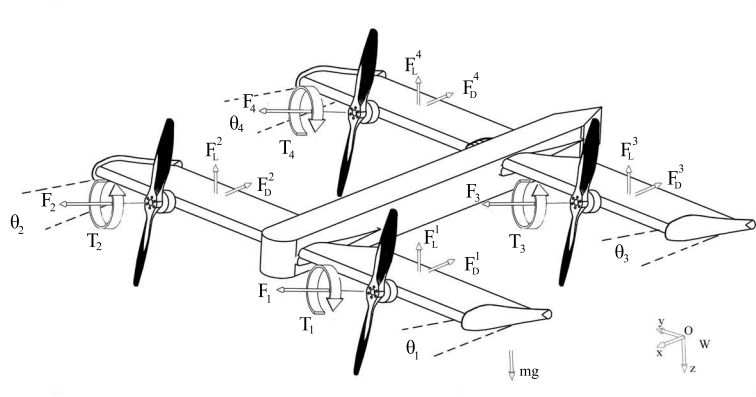


Figure 3.2: External forces and torques acting on the vehicle

External Forces

The total external force F_t acting on the vehicle's center of gravity is the sum of the forces F_{th} created by the rotors, the gravity F_g , the lift and drag forces generated by the wings F_w and the aerodynamic forces F_d which is considered as a disturbance.

$$F_t = F_g + F_w + F_{th} + F_d \quad (5)$$

Gravity

The gravitational acceleration acting on the vehicle is a fixed vector along z_w axis on the earth reference frame W . The gravitational force therefore is a function of roll and pitch angles if expressed in the body frame B :

$$F_g = \begin{bmatrix} -s_\theta \\ s_\phi c_\theta \\ c_\phi c_\theta \end{bmatrix} mg$$

Wing Forces

Wing forces forming due to vehicle's flight speed incorporate the lift and drag forces created by each of four wings separately. On a fixed wing airplane the aerodynamic forces are modeled with a conventional lift and drag coefficient approach that assumes constant angle of attack during flight [40], whereas on a rotary wing airplane the blade element theory is used which takes into account the variation of angle of attack. However these models do mainly consider the before stall flight envelope and it is hard to find tables of lift and drag coefficients up to angles of attack of 90° . The airfoil of NACA2410 wing profile is obtained by [52] for degrees 0-20. The after

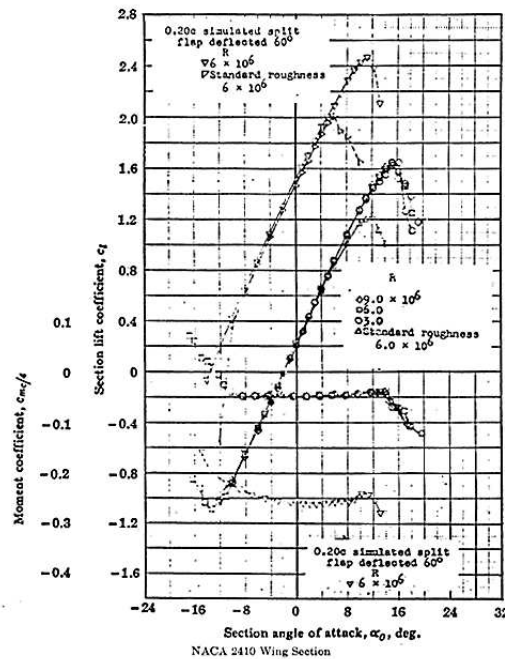


Figure 3.3: NACA2410 airfoil

stall region shows different characteristics for different Reynolds' Numbers. For low Reynolds' Numbers the lift continues to increase with the angle

of attack and the drop of lift on stall angle is smoother (Fig. 3.4 [52]). Besides that, in order to incorporate the transition process in aerodynamic

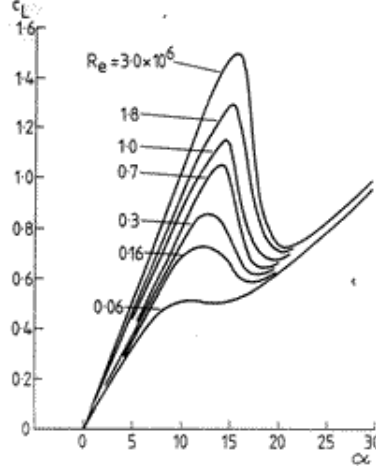


Figure 3.4: Lift vs. Reynolds' number

forces, the lift function $F_L(\theta_i, v_x, v_z)$ and the drag function $F_D(\theta_i, v_x, v_z)$ are modeled as not just functions of forward linear velocity v_x but also functions of ascend/descend velocity v_z of the vehicle, namely

$$\begin{bmatrix} F_D \\ 0 \\ F_L \end{bmatrix} = R(\theta_i) \begin{bmatrix} -\frac{1}{2}c_D(\alpha_i)\rho Av_\alpha^2 \\ 0 \\ -\frac{1}{2}c_L(\alpha_i)\rho Av_\alpha^2 \end{bmatrix}$$

where

$$v_\alpha = \sqrt{v_x^2 + v_z^2}$$

$$\alpha_i = \theta_i - (-atan2(v_z, v_x))$$

Here ρ is the air density, A is the wing area, v_α is the airstream velocity and α_i is the effective angle of attack as shown in Fig. 3.5. The $R(\theta_i)$ is the rotation matrix around y axis to transform the lift and drag forces back to

the body frame.

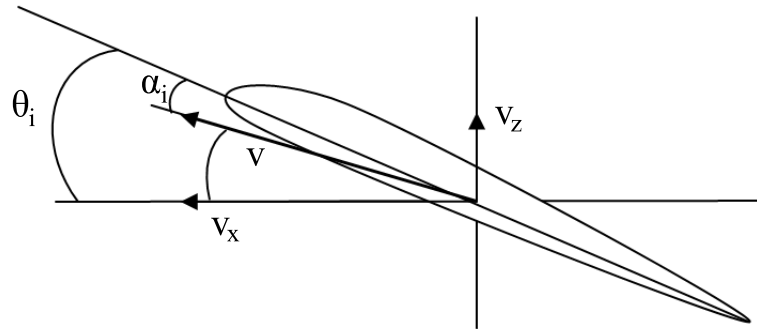


Figure 3.5: Effective angle of attack α_i

The lift coefficient $c_L(\alpha_i)$ and drag coefficient $c_D(\alpha_i)$ are modeled according to the data points obtained from Javafoil and airfoil models from [52], [53].

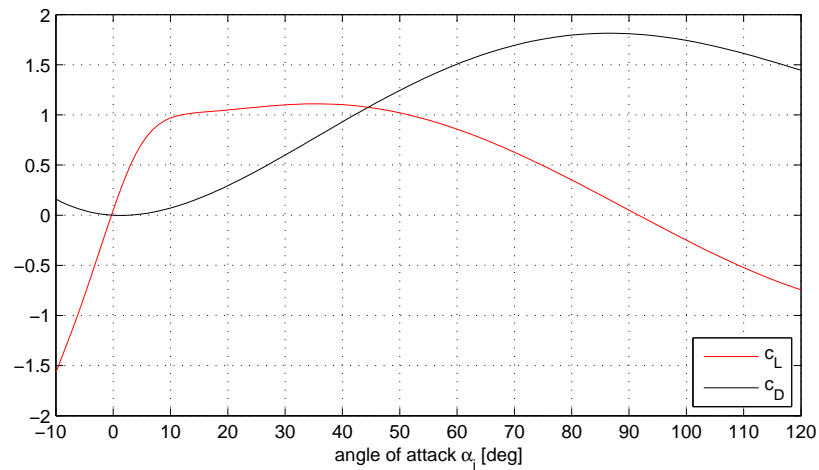


Figure 3.6: Lift and Drag coefficients on large angles of attack

Fig. 3.7 and Fig. 3.8 show the variation of lift and drag forces versus tilt angle θ_i and airstream velocity.

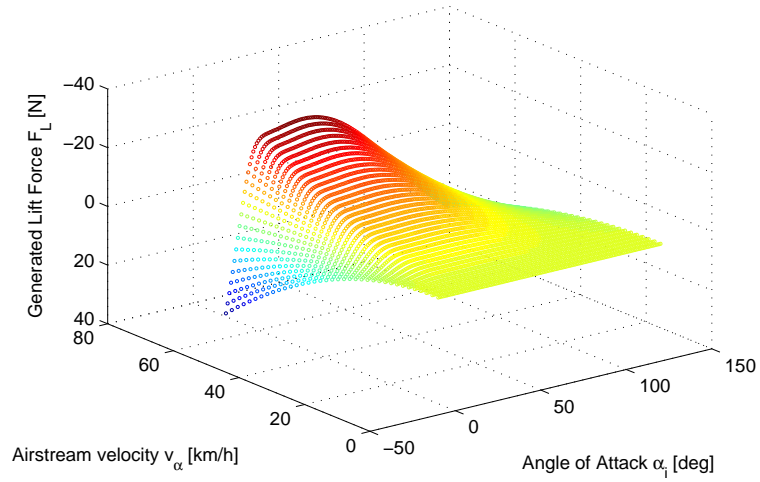


Figure 3.7: Lift force F_L

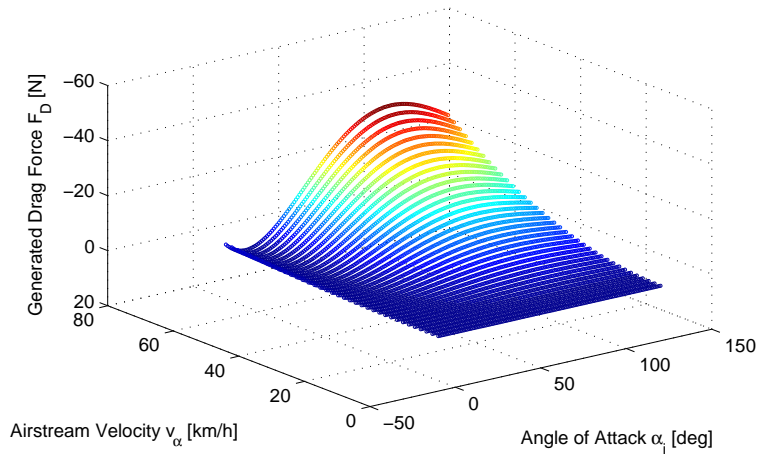


Figure 3.8: Drag force F_D

The sum of lift and drag forces are then formulated in body frame B as

$$F_w = \begin{bmatrix} F_D(\theta_1, v_x, v_z) + F_D(\theta_2, v_x, v_z) + F_D(\theta_3, v_x, v_z) + F_D(\theta_4, v_x, v_z) \\ 0 \\ F_L(\theta_1, v_x, v_z) + F_L(\theta_2, v_x, v_z) + F_L(\theta_3, v_x, v_z) + F_L(\theta_4, v_x, v_z) \end{bmatrix}$$

It is important to mention that the wings at the back are rotated together and their angle of attacks are the same for all time ($\theta_3 = \theta_4$).

Actuation Forces (Rotor Forces)

From experimental data the relationship between the thrust and square of propeller angular velocity (ω^2) is verified to be very close to linear (Fig. 3.9). With the assumption of near hover flight (low airspeed) the propeller

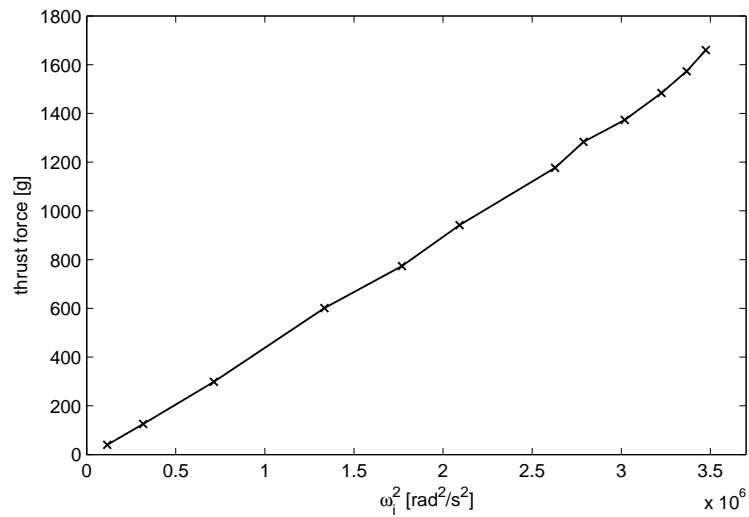


Figure 3.9: Relationship between thrust and square of angular velocity for 14x7 propeller

thrusters $F_{(1,2,3,4)}$ are modeled as,

$$F_i = k\omega_i^2$$

With the tilt angles θ_i of the wings taken into account, the actuation forces for all flight modes are obtained as,

$$F_{th} = \begin{bmatrix} c_{\theta_1} & c_{\theta_2} & c_{\theta_3} & c_{\theta_3} \\ 0 & 0 & 0 & 0 \\ -s_{\theta_1} & -s_{\theta_2} & -s_{\theta_3} & -s_{\theta_3} \end{bmatrix} \begin{bmatrix} k\omega_1^2 \\ k\omega_2^2 \\ k\omega_3^2 \\ k\omega_4^2 \end{bmatrix} \quad (6)$$

External Torques

The total external torque M_t acting on the vehicle's center of gravity is the sum of the torques M_{th} created by the rotors M_w created by the drag/lift forces of the wings, M_{gyro} created by the gyroscopic effects of the propellers and the aerodynamic torques M_d which is considered as a disturbance. The dynamic model contains the gyroscopic effects due to the propellers rotation whereas the body gyroscopic effects are considered to be negligible due to the slow nature of rotational motions during flight.

$$M_t = M_{gyro} + M_w + M_{th} + M_d \quad (7)$$

Gyroscopic Torques

The gyroscopic torques arise due to the change of the plane of rotation of a rotating object. This torque has much more dynamic effect on objects that rotate on very high speeds. Because of that the propellers gyroscopic torques need to be included in the dynamic model. By modeling the gyroscopic effect of the propellers it is assumed that the transition process is slow enough such that the rate of the change of angle of attacks due to transition cause

negligible effects. The gyroscopic torques in body frame B are modeled as,

$$M_{gyro} = \sum_{i=1}^4 J[\eta_i \Omega_b \times \begin{bmatrix} c\theta_i \\ 0 \\ -s\theta_i \end{bmatrix} \omega_i]$$

$$\eta_{(1,2,3,4)} = 1, -1, -1, 1$$

Here J is the moment of inertia of the propeller measured along the axis of propeller's rotation.

Aerodynamic Torques

The torques that arise due to the imbalance of the lift and drag forces created by the wings are defined as aerodynamic torques. With the assumption of that the lift and drag can be considered as acting on a single point on the surface of the wing that lies almost in the middle of the wingspan and at the 25% chord length, the torques acting due to lift and drag forces can be modeled as,

$$M_w = \begin{bmatrix} (F_L(\theta_1, v_x, v_z) - F_L(\theta_2, v_x, v_z))l_s \\ (F_L(\theta_1, v_x, v_z) + F_L(\theta_2, v_x, v_z) - F_L(\theta_3, v_x, v_z) - F_L(\theta_4, v_x, v_z))l_l \\ (-F_D(\theta_1, v_x, v_z) + F_D(\theta_2, v_x, v_z))l_s \end{bmatrix}$$

Actuation Torques (Rotor Torques)

The actuation torques are composed of two components. First component is the sum of torques that are created by the rotors inherently and that are proportional to the thrust. Second component is the due to the imbalance of

thrust forces acting on different tilt angles with different magnitudes. These two components of actuation torques can be formulated as,

$$M_{th} = \begin{bmatrix} l_s s_{\theta_1} & -l_s s_{\theta_2} & l_s s_{\theta_3} & -l_s s_{\theta_4} \\ l_l s_{\theta_1} & l_l s_{\theta_2} & -l_l s_{\theta_3} & -l_l s_{\theta_4} \\ l_s c_{\theta_2} & -l_s c_{\theta_2} & l_s c_{\theta_3} & -l_s c_{\theta_4} \end{bmatrix} \begin{bmatrix} k\omega_1^2 \\ k\omega_2^2 \\ k\omega_3^2 \\ k\omega_4^2 \end{bmatrix} + \begin{bmatrix} -c_{\theta_1} & -c_{\theta_2} & -c_{\theta_3} & -c_{\theta_4} \\ 0 & 0 & 0 & 0 \\ s_{\theta_1} & s_{\theta_2} & s_{\theta_3} & s_{\theta_4} \end{bmatrix} \begin{bmatrix} \lambda_1 k\omega_1^2 \\ \lambda_2 k\omega_2^2 \\ \lambda_3 k\omega_3^2 \\ \lambda_4 k\omega_4^2 \end{bmatrix} \quad (8)$$

Note that the torque created by the rotors is proportional to the thrust, with a constant ratio λ_i that depends on the propeller geometry,

$$T_i = \lambda_i k\omega_i^2$$

It is also important to mention that the sum of torques created by the rotors result in a roll moment along the x axis in horizontal flight mode ($\theta_{1,2,3,4} = 0$) and in a yaw moment along the z axis in vertical flight mode ($\theta_{1,2,3,4} = \pi/2$).

Chapter IV

4 Controller Synthesis

4.1 Background

Several different controllers designed for the VTOL vehicles with quad-rotor configurations exist in the literature. In their work, Bouabdallah et al. present a PID controller for a simplified model and an LQ controller for a more complete model [54]. Besides classical PID controllers used in [55], PD [56] and quaternion based PD^2 [57] controllers are also used in quad-rotor research. [58] and [59] show the result of optimal controllers based on LQR and State Dependent Riccati Equation. In [60] Earl and D'Andrea develop an attitude estimation technique by using a decomposition approach. Another study is carried out to use an output feedback controller with estimators and observers in [61]. Backstepping control of Madani and Benallegue [62] is a recent example of recent non-linear control methods applied on quad-rotors. In [63] a comparison of two nonlinear controllers based on integral sliding mode and reinforcement learning are presented. Hably and Merchand have recently proposed a global asymptotic stabilizing controller under bounded inputs [64]. Another recent study proposes a scheme for full control of quad-rotors [65]. Other controllers for quad-rotor control and stabilization can be found in [66], [67], and [68].

4.2 Controller Design in Linear Framework

To design attitude and position controllers for VTOL mode of the aerial vehicle, first the equations obtained in Chapter III are put into state-space form. The state vector X consists of the position (P), the attitude (α), the linear velocity (V_b) and the angular velocity (ω_b).

$$X = \begin{bmatrix} P_w \\ V_b \\ \omega_b \\ \alpha_w \end{bmatrix} \quad (1)$$

In light of equations (1)-(4) we have

$$\dot{X} = \begin{bmatrix} \dot{P}_w \\ \dot{V}_b \\ \dot{\omega}_b \\ \dot{\alpha}_w \end{bmatrix} = \begin{bmatrix} R^{-1}(\alpha_w) \cdot V_b \\ \frac{1}{m} \cdot [F_t - \omega_b \times (m \cdot V_b)] \\ I_b^{-1} \cdot [M_t - \omega_b \times (I_b \cdot \omega_b)] \\ E^{-1}(\alpha_w) \cdot \omega_b \end{bmatrix} \quad (2)$$

which is a nonlinear plant of the form

$$\dot{X} = f(X, u) \quad (3)$$

In order to simplify the controller design, the actuating forces and torques are decomposed into four virtual control inputs (u_i) as follows:

$$u = \begin{bmatrix} u_1 \\ u_2 \\ u_3 \\ u_4 \end{bmatrix} = \begin{bmatrix} -(F_1 + F_2 + F_3 + F_4) \\ l_s \cdot [(F_1 + F_3) - (F_2 + F_4)] \\ l_l \cdot [(F_1 + F_2) - (F_3 + F_4)] \\ \lambda_1 F_1 + \lambda_2 F_2 + \lambda_3 F_3 + \lambda_4 F_4 \end{bmatrix} \quad (4)$$

It is important to mention that this decomposition is valid only for the VTOL mode of the aerial vehicle with 4 DOF actuation. For the horizontal flight mode the actuation becomes 5 DOF because of the force component in x_b direction and a different decomposition method needs to be applied.

4.2.1 PID Attitude Stabilization

The PID Controllers are used very widely because of their simplicity and provide satisfactory performance for many plants. Therefore a PID controller structure is implemented to stabilize the attitude of SUAVI is for vertical flight experiments. The transfer functions for the roll, pitch and yaw of the plant are obtained from linearization of the dynamic model around hover condition (no gyroscopic effects),

$$\ddot{\phi} = \frac{u_2}{I_x} \quad (5)$$

$$\ddot{\theta} = \frac{u_3}{I_y} \quad (6)$$

$$\ddot{\psi} = \frac{u_4}{I_z} \quad (7)$$

A PID controller is mathematically formulated as,

$$u(t) = K_p e(t) + K_i \int_0^t e(\tau) d\tau + K_d \frac{de(t)}{dt} \quad (8)$$

with tuning parameters K_p , K_i and K_d , where the error $e(t)$ is defined as

$$e(t) = X_{ref} - X(t) \quad (9)$$

The K_p term contributes proportional to the error and influences the bandwidth and rise time characteristics of the controller. For large bandwidth the trade-off is often an increased overshoot at the output. The K_i term eliminates steady-state error, however it can introduce oscillations to the system. The K_d term dampens the response of the system by changing the overshoot and rise-time behavior of the system. Although this controller structure works well in theory, for a robust implementation two modifications are necessary to apply on the PID controller. Firstly the derivative action of the PID controller needs to be modified such that for a step reference the derivative term will not result to an impulse at the output. If that happens, a saturation due to the physical limitations of the motors is very probable and therefore not desired. To eliminate this problem instead of the time derivative of $e(t)$ the time derivative of the state X is used.

$$u(t) = K_p e(t) + K_i \int_0^t e(\tau) d\tau - K_d \frac{dX(t)}{dt} \quad (10)$$

Secondly, a windup because of integral action may also occur which can dominate the proportional and derivative actions. To overcome this a saturation is applied to the integral term of the controller. The final form of the PID controller is given in Fig. 4.1.

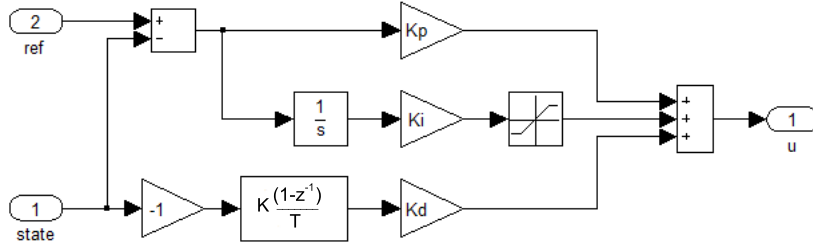


Figure 4.1: Block diagram of the PID controller

4.2.2 PID Position Controller

The linear motions along x and y axes of the aerial vehicle are coupled with the pitch and roll angles. In order to accelerate in positive x direction a negative pitch angle needs to be applied. Similar, in order to accelerate in positive y direction a positive roll angle needs to be applied. Therefore the position control in xy plane can be controlled with cascaded PID controllers. For altitude control no cascade structure is needed, control along z axis is applied on the plant:

$$\ddot{z} = (\cos(\theta)\cos(\phi))\frac{u_1}{m} + g \quad (11)$$

If linearized around hover conditions ($\theta, \phi = 0$), the altitude model will be a second order differential equation similar to equations (5, 6, 7), namely

$$\ddot{z} = \frac{u_1}{m} + g \quad (12)$$

The resulting structure of cascade position controller is given in Fig. 4.2

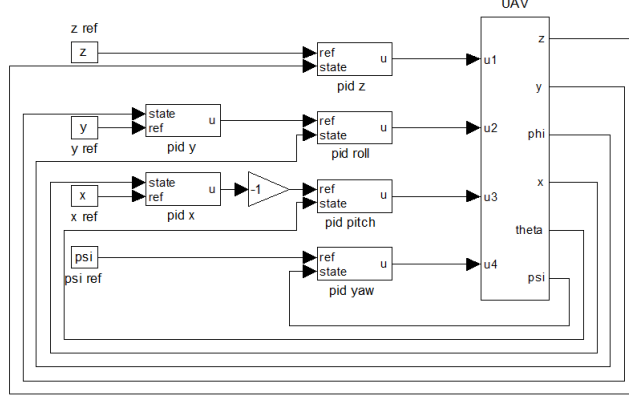


Figure 4.2: Block diagram of cascade PID position controller

4.2.3 LQR Position Controller

Although the state vector contains 12 variables, in VTOL mode the aerial vehicle is an underactuated system with 4 DOF. Therefore the control parameters of the plant are chosen to be the position $P(x, y, z)$ and yaw angle (ψ), for LQR controller design. The dynamic equations of the vehicle are linearized symbolically using MAPLE. A , B and C matrices of the linearized system are computed as follows:

$$A = \begin{bmatrix} \frac{\partial f_1(X,u)}{\partial X_1|_{x=x_n}} & \dots & \frac{\partial f_1(X,u)}{\partial X_{12}|_{x=x_n}} \\ \vdots & \ddots & \vdots \\ \frac{\partial f_{12}(X,u)}{\partial X_1|_{x=x_n}} & \dots & \frac{\partial f_{12}(X,u)}{\partial X_{12}|_{x=x_n}} \end{bmatrix}$$

$$B = \begin{bmatrix} \frac{\partial f_1(X,u)}{\partial u_1|_{u=u_n}} & \dots & \frac{\partial f_1(X,u)}{\partial u_4|_{u=u_n}} \\ \vdots & \ddots & \vdots \\ \frac{\partial f_{12}(X,u)}{\partial u_1|_{u=u_n}} & \dots & \frac{\partial f_{12}(X,u)}{\partial u_4|_{u=u_n}} \end{bmatrix}$$

$$C = I$$

where I is 12×12 identity matrix. The linear model for any operating point can be obtained by putting the states of the operating point into the linear model matrices. After obtaining the desired linear model a controller in the form:

$$u(t) = -K(X(t) - X_{ref}) \quad (13)$$

is selected to stabilize the system, where X_{ref} is the reference state. The feedback gain matrix K is found by minimizing the following cost function

$$J = \int_0^{\infty} [(X(t) - X_{ref})^T Q (X(t) - X_{ref}) + u(t)^T R u(t)] dt \quad (14)$$

where Q and R matrices are semi-positive definite and positive definite weight matrices of the state and control variables respectively. Solution of the minimization problem implies the well known Riccati equation,

$$PA + A^T P + Q - PBR^{-1}B^T P = 0 \quad (15)$$

which in turn implies

$$K = R^{-1}BP \quad (16)$$

By tuning the Q and R matrices the reference tracking characteristics and control effort characteristics can be determined for each state variables and control variables independently.

The K gains of the LQR controller are calculated for each 4° increment of yaw (ψ) angles in 360° , for a full range control of yaw angle. This way an interpolation of K gains according to the yaw angle of the vehicle is accomplished. The structure of the LQR controller is given in Fig. 4.3.

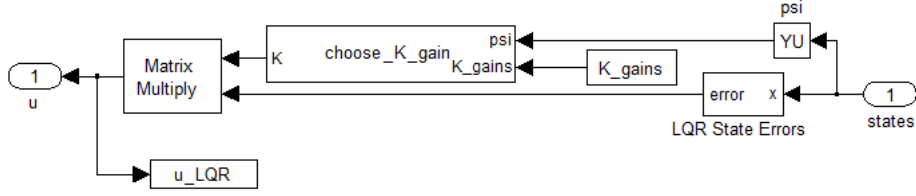


Figure 4.3: Block diagram of the LQR controller

4.3 Transition Between Vertical Flight and Horizontal Flight

The transition process between vertical and horizontal flight modes is established under the assumptions of synchronous change of angle of attacks ($\theta_1 = \theta_2 = \theta_3 = \theta_4$). The altitude control input u_1 consists of the total lift force generated by propeller thrusts and aerodynamic lift forces. Referring to the forces derived in Chapter III, the aerodynamic lift force F_{Lift} is calculated as a function of v_x , v_y and θ_i , namely

$$F_{Lift} = F_L^1 + F_L^2 + F_L^3 + F_L^4 \quad (17)$$

For transition mode the altitude control input u_1 is modified by subtracting F_{Lift} from u_1 such that u_1 only consists of the thrust component along z direction in the presence of a tilt angle.

$$\hat{u}_1 = u_1 - F_{Lift} \quad (18)$$

The z and x components of the thrust force F_i are shown in Fig. 4.4. The control inputs $u_{2,3,4}$ of attitude stabilization are fed to the system without any modification. Similar to virtual input decomposition for VTOL mode ($\theta_i = 90^\circ$) in equation (4), a new control input matrix involving tilt angles is

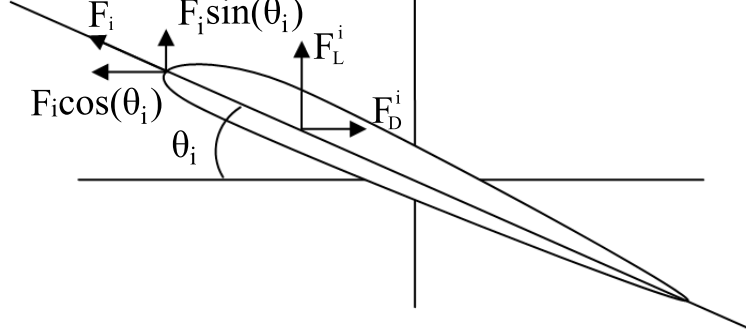


Figure 4.4: Forces acting during transition

obtained from equations (6) and (8), namely

$$\hat{u} = \begin{bmatrix} \hat{u}_1 \\ u_2 \\ u_3 \\ u_4 \end{bmatrix} = \begin{bmatrix} -s_{\theta_1} & -s_{\theta_2} & -s_{\theta_3} & -s_{\theta_4} \\ l_s s_{\theta_1} - \lambda_1 c_{\theta_1} & -l_s s_{\theta_2} - \lambda_2 c_{\theta_2} & l_s s_{\theta_3} - \lambda_3 c_{\theta_3} & -l_s s_{\theta_4} - \lambda_4 c_{\theta_4} \\ l_l s_{\theta_1} & l_l s_{\theta_2} & -l_l s_{\theta_3} & -l_l s_{\theta_4} \\ l_s c_{\theta_2} + \lambda_1 s_{\theta_1} & -l_s c_{\theta_2} + \lambda_2 s_{\theta_2} & l_s c_{\theta_3} + \lambda_3 s_{\theta_3} & -l_s c_{\theta_4} + \lambda_4 s_{\theta_4} \end{bmatrix} \begin{bmatrix} F_1 \\ F_2 \\ F_3 \\ F_4 \end{bmatrix} \quad (19)$$

The thrust forces are obtained by using the inverse of 4x4 matrix in equation (19). With this approach during a transition from vertical to horizontal flight mode the altitude of the vehicle is maintained by transferring the lift from rotor thrust to aerodynamic lift generated by wings. A first draft of the proposed transition controller will appear in [69].

4.4 Attitude Estimation Using Kalman Filtering

Kalman filters within quaternion framework [70], extended Kalman filters [71] with nonlinear dynamics and sigma point Kalman filters [72] have been implemented in the literature for attitude estimation. These filters incorporate highly coupled rotational dynamics and require cumbersome Jacobian

calculations which are hard to implement for real-time processing in a microprocessor unit. Feasible options are complementary filters [73, 74], 1D Kalman filters [75] and stabilized angle calculations [76] that give fast and useful attitude estimations around hover conditions. In order to implement a robust attitude estimator the gyroscope, accelerometer and magnetometer characteristics of Sparkfun IMU are explored.

Gyroscopes

A gyroscope outputs the magnitude of rotational velocity around its axis and this output can be used to find the angle of rotation around that axis via integration methods. The IDG300 gyroscopes from InvenSense output the rotational velocities up to 500 deg/sec [77] with a bandwidth of 96 Hz [38]. In ideal conditions the zero rotational velocity corresponds to a digital output of 512 whereas a ± 500 deg/sec rotational velocity corresponds to 0-1023 readings. As the ideal conditions do not hold in reality, with several experiments it is shown that the zero rotational velocity readings range between 450 and 550 (Fig.4.5).

The gyroscope readings in static environment have shown very good noise characteristics which are bounded by ± 2 increments from the mean value of 0 rotational velocity. The noise characteristics of the gyroscopes are also investigated on the aerial vehicle with four rotors running. It is observed that the high frequency vibrations do not affect the gyroscope sensitivity in a great manner and the jitter is bounded by ± 5 increments (Fig. 4.6).

In several measurements it is observed that the mean value of 0 rotational velocity drifts ± 15 increments from the initial value over as short as 50

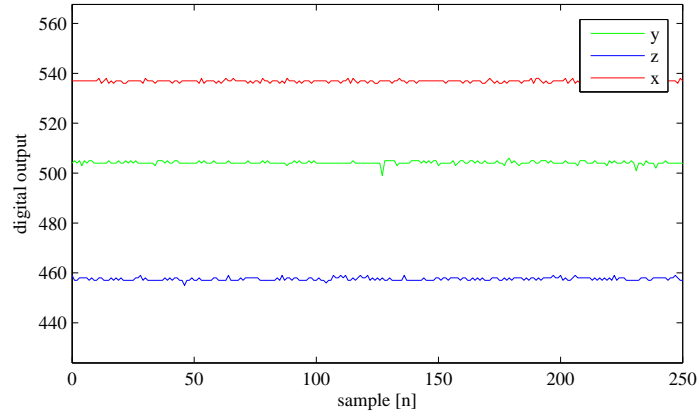


Figure 4.5: Gyroscope readings around x,y,z axes

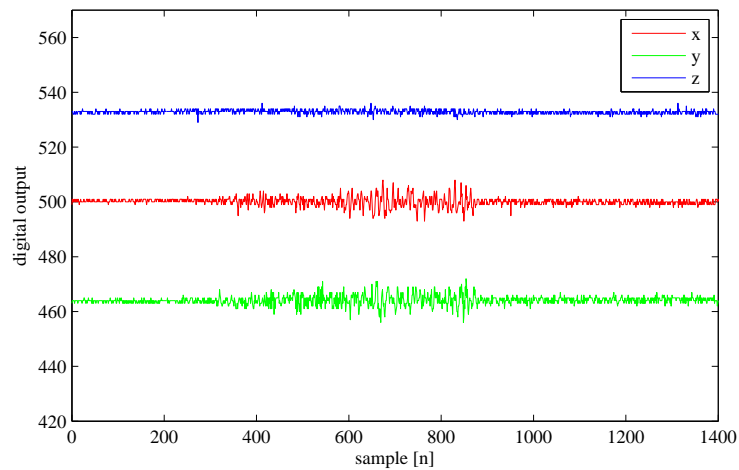


Figure 4.6: Gyroscope readings around x,y,z axes while rotors are running

sec runtime. Because this drift problem is unavoidable, the integration of rotational velocity causes to an accumulative error in angle estimation. A compensation method for the drift problem such as Kalman filtering [78] or complementary filtering [74] is necessary for a good attitude estimation.

Accelerometers

An accelerometer outputs the magnitude of acceleration acting on its axis. Therefore the gravity vector which is pointing down to the center of the earth can be used to find the roll and pitch angles using three accelerometer readings. In a static environment where there is no acceleration due to the external forces acting on the sensors, the roll and pitch angles can be estimated very precisely. The sensory data from MMAQ7260 accelerometers in the Sparkfun IMU V4 are available with an output bandwidth of 350 Hz for the x and y axes, and 150 Hz for the z axis [38]. However the accelerometers are very sensitive to high frequency noise and they require very narrow bandwidth low pass filters in order to eliminate the noise effects. That results to a slow response compared to gyroscope measurements.

The MMAQ7260 accelerometers can output accelerations up to 6g [79] whereas 1.5g, 2g and 4g sensitivity levels are also selectable for better precision. Using the 1.5 g setting for the best precision, 1 g acceleration reading is expected to be 853 on a 0-1023 scale ideally. However, in experiments under static environment conditions, it is observed that the 1 g acceleration of the earth resulted to a sensor reading of 750 (Fig. 4.7).

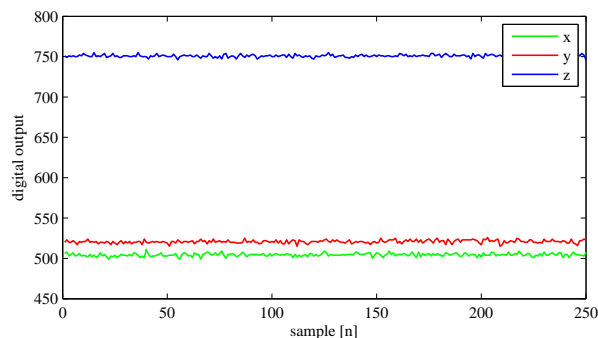


Figure 4.7: Accelerometer readings around x,y,z axes

In several experiments it is observed that the noise characteristics of the accelerometers under static conditions have high S/N ratio (Fig. 4.7), but under high frequency vibrations (while rotors are running) the measurements become useless (Fig. 4.8). Therefore a low pass filter with 10 Hz cut-off

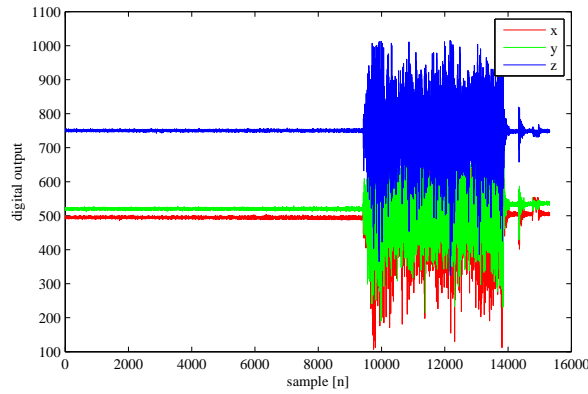


Figure 4.8: Accelerometer readings around x,y,z axes during hover

frequency is added to the circuit before analog to digital conversion and the S/N ratio is improved as seen in Fig. 4.9. To obtain a higher S/N Ratio the cut-off frequency of the low pass filter is changed to 0.6 Hz. Fig. 4.10 below shows the clean accelerometer measurement data during hover.

Magnetometers

Magnetometers measure the magnetic field strength and with a 3-axis magnetometer the magnetic field vector showing the North Pole of earth can be obtained. Honeywell HMC1053 magnetometers measure the magnetic field with a sensitivity of 3.3mV/Gauss on 3.3 V operating voltage [80]. This signal is then amplified on Sparkfun IMU sensor board with an op-amp by 100 to 0.33 V/Gauss [38]. According to NOAA[81] the earth's magnetic field

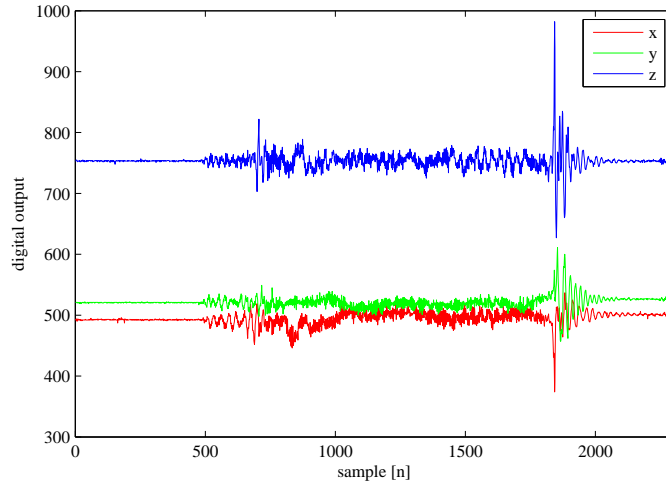


Figure 4.9: Accelerometer readings around x,y,z axes with 10 Hz low pass filter during hover

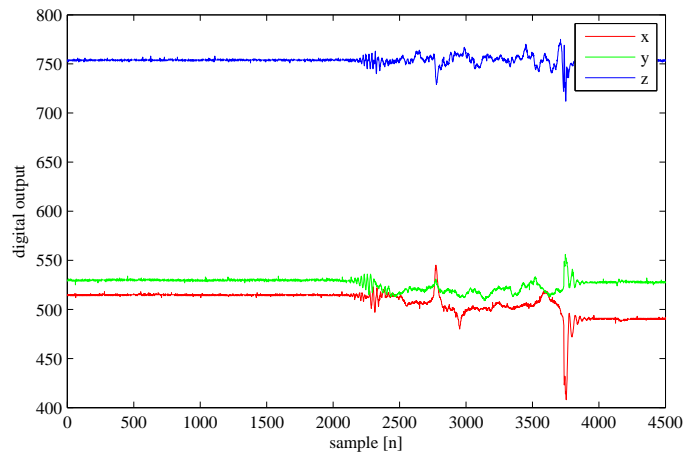


Figure 4.10: Accelerometer readings around x,y,z axes with 0.6 Hz low pass filter during hover

at the location of the laboratory has a horizontal intensity of 24,725.2 nT which corresponds to ~ 0.25 Gauss. A 0.25 Gauss reading on a single axis would show up as 0.0825 V which corresponds to 15 steps in analog to digital

conversion. Thus for a 360° yaw turn in horizontal plane an x-y plot of a circle with 30 step radius is expected. Several experiments have shown that the magnetometer measurements are heavily affected by inherent noise. The jitters magnitude go up to ± 10 steps which is almost 66% of the maximum measurement we can obtain. Such a low S/N Ratio gives very poor yaw estimation. Low pass filters with very small bandwidth need to be used.

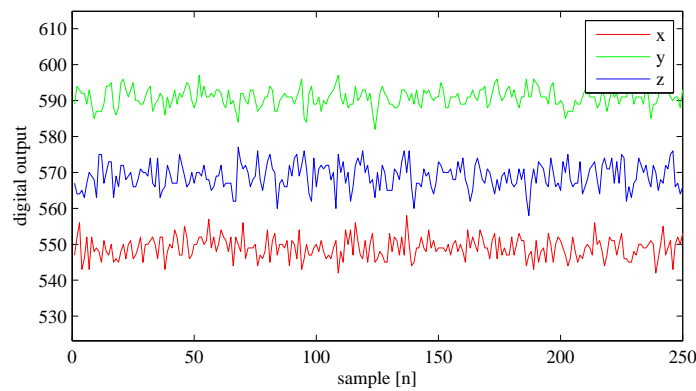


Figure 4.11: Magnetometer readings around x,y,z axes

Kalman Filtering

Kalman Filter uses a combination of gyroscopes and accelerometers readings to provide robust angle estimations. The key characteristics are, accelerometers introduce a phase delay because of low-pass filters, but the calculated angles do not drift over time, whereas gyroscopes give good angle estimations in short time intervals. As one can see from Fig. 4.12, the integration of rotational velocity from gyroscopes results in a drift in angle estimation especially after repetitive cyclic motions. To obtain roll and pitch angles of the aerial vehicle two 1D Kalman Filters are implemented with

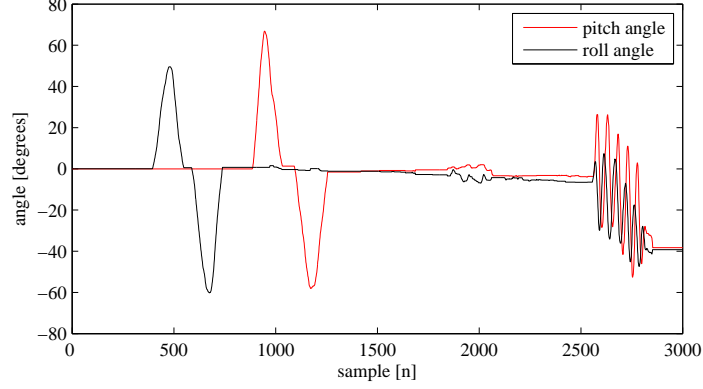


Figure 4.12: Roll and pitch angles obtained via integration

the assumption of negligible coupling between roll and pitch angles in hover condition. For the linear dynamic model in the form

$$x_{k+1} = Ax_k + Bu_k$$

the discretized model of the angle integration from gyroscope data is obtained as:

$$\begin{bmatrix} angle \\ bias \end{bmatrix}_{k+1} = \begin{bmatrix} 1 & -T \\ 0 & 1 \end{bmatrix} \begin{bmatrix} angle \\ bias \end{bmatrix}_k + \begin{bmatrix} T \\ 0 \end{bmatrix} u_k \quad (20)$$

In this equation T is the sampling time of the system, u_k is the gyroscope output at $t = kT$ and the state vector contains the estimated angle and the bias. The Kalman filter is to correct the bias term after each iteration by comparing estimated angle with the angle obtained from accelerometer measurements. The filter consists of prediction and correction stages. The prediction stage is formulated as [78]:

$$\hat{x}_k^- = A\hat{x}_{k-1} + Bu_{k-1}$$

$$P_k^- = AP_{k-1}A^T + Q$$

The error covariance matrix P_k^- and state vector \hat{x}_k^- from prediction stage are then used to calculate the Kalman gain K and prediction in the correction stage as:

$$K_k = P_k^- H^T (HP_k^- H^T + R)^{-1}$$

$$\hat{x}_k = \hat{x}_k^- + K_k(z_k - H\hat{x}_k^-)$$

$$P_k = (I - K_k H)P_k^-$$

The Q and R matrices in Kalman filter equations are process noise covariance and measurement covariance matrices respectively. Filter performance can be improved tuning these parameters. Using the above explained equations two separate one dimensional Kalman Filters are implemented in microprocessor unit to estimate roll and pitch angles of the vehicle. As seen in Fig. 4.13 the drift problem is eliminated.

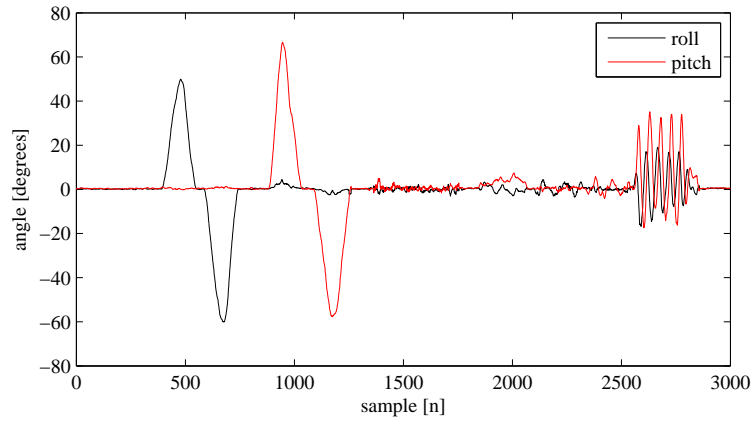


Figure 4.13: Roll and pitch angles obtained with Kalman filters

4.5 Simulations

The nonlinear dynamic model derived in Chapter III is implemented in Simulink/MATLAB environment (Fig. 4.14).

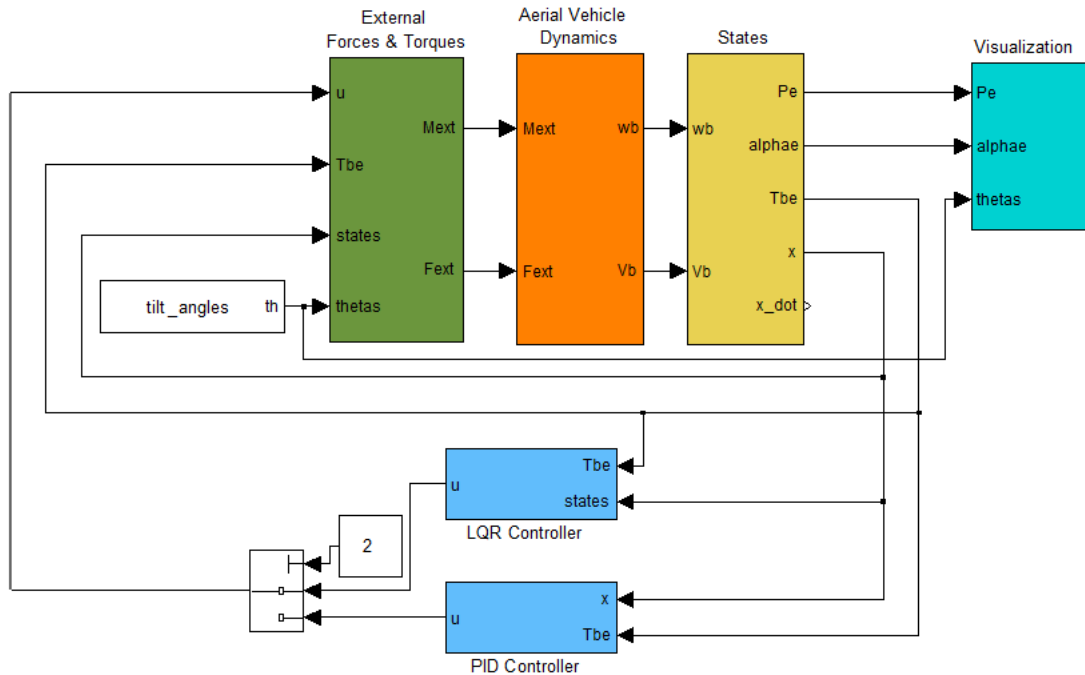


Figure 4.14: Simulink model of the SUAVI

With this simulation model, switching between different controllers is possible for performance evaluation.

4.5.1 Visualization Using VR Toolbox

An important part of the simulation environment is the developed Visualization Toolbox. Using the CAD drawing of the aerial vehicle a vrml model is created in VRealm Builder Environment which is integrated with VR Toolbox of Matlab.

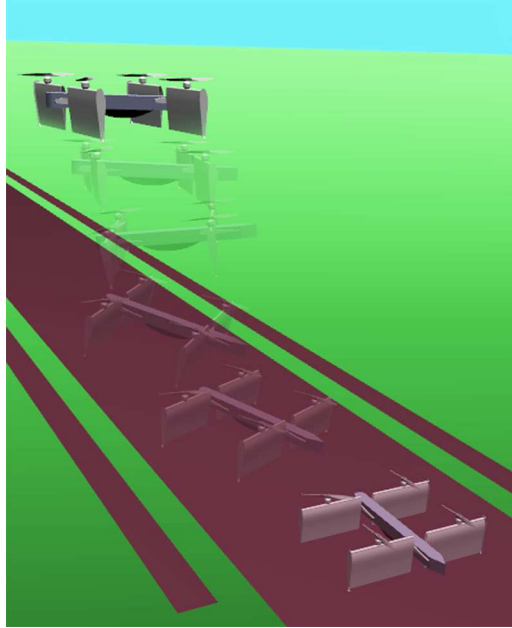


Figure 4.15: Take-Off visualization using VR toolbox

This visual model is connected to the dynamic model of the aerial vehicle through Simulink and the simulations are visualized in real-time with the update of actual attitude and position parameters along the wing tilt angles.

With the help of this visualization toolbox the vehicle dynamics can easily be observed and the performance evaluations can easily be made. The point of view of visualization can be fixed such that it will move with the Body Frame B or remain in place bound to the world frame W for different analysis of the aerial vehicle.

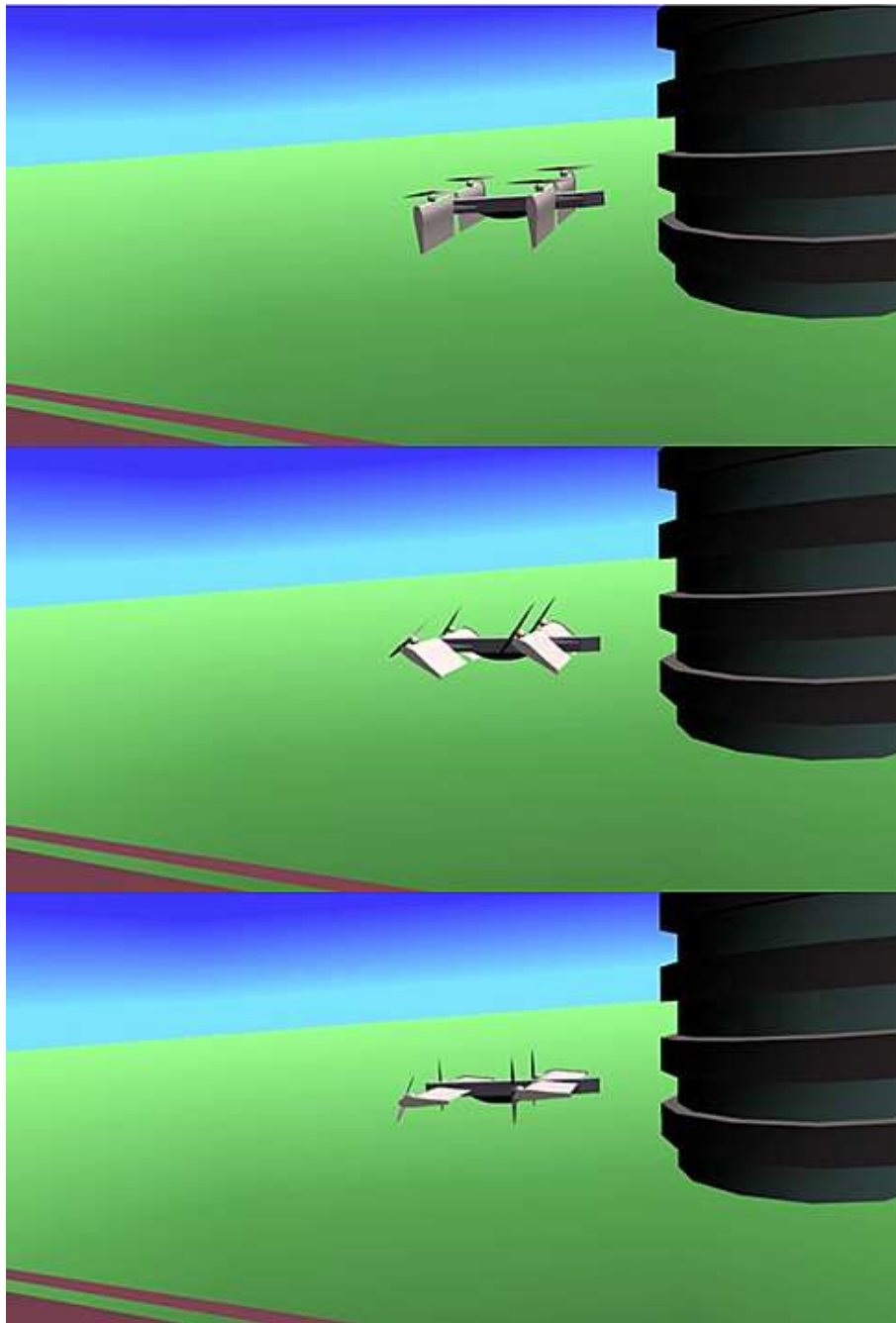


Figure 4.16: Flight modes visualization using VR toolbox

4.5.2 Simulation Results

PID Controller Simulations

The performance of the PID controller is evaluated on the nonlinear dynamic model of the vehicle given by (2) in MATLAB/Simulink. The controller variables K_p, K_i and K_d for roll, pitch, yaw and altitude control are selected as,

$$\begin{aligned} \text{Roll: } & K_p = 1, K_i = 0.001, K_d = 0.5 \\ \text{Pitch: } & K_p = 1, K_i = 0.001, K_d = 0.5 \\ \text{Yaw: } & K_p = 0.5, K_i = 0.001, K_d = 0.9 \end{aligned}$$

Starting with the initial configuration $P_w = (0, 0, 0)^T$ and $\alpha_w = (0, 0, 0)^T$ of the vehicle, the simulation results given in Fig. 4.17 show the variation of the attitude variables under random disturbance for the reference inputs given from joystick inputs.

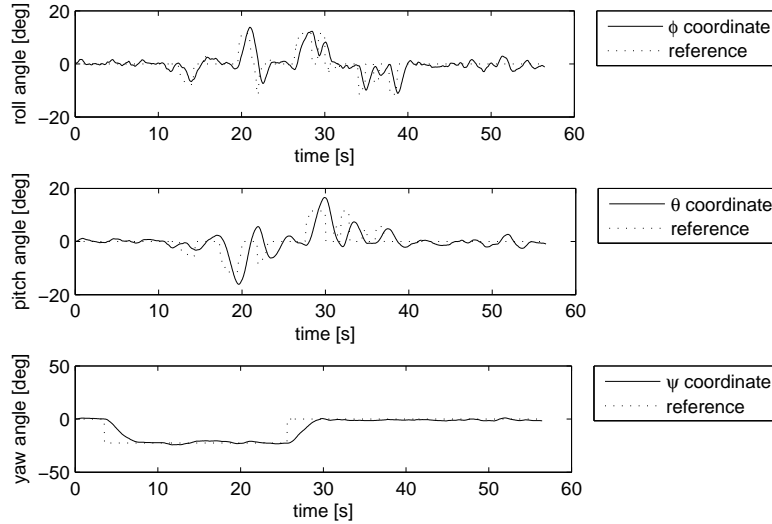


Figure 4.17: Attitude control using PID

Note that position and angle references are tracked with small steady state errors and the tracking response of roll and pitch angles from user inputs is fast enough to achieve desired maneuvers. The lift forces generated by each rotor for this controller are shown in Fig. 4.18.

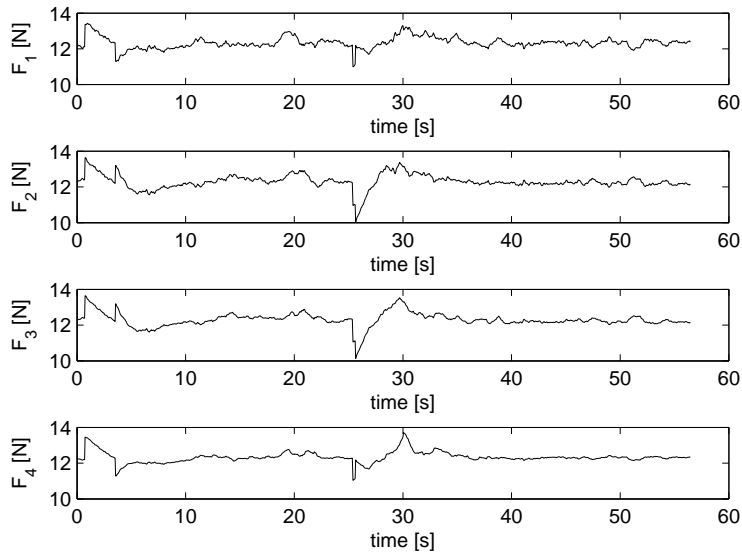


Figure 4.18: Forces created by rotors (PID)

The control effort is bounded by ± 2 N from the nominal thrust, and is in the physical limitations of the rotor thrust.

The PID attitude stabilization keeps the vehicle in level during flight however drifting along x and y directions is unavoidable with this controller alone. To keep the aerial vehicle stationary cascade PID structure that controls the x and y position of the vehicle over pitch and roll angles is used. Fig. 4.19 and 4.20 show the stabilization of attitude over $P_{ref} = (0, 0, 0)^T$ position reference.

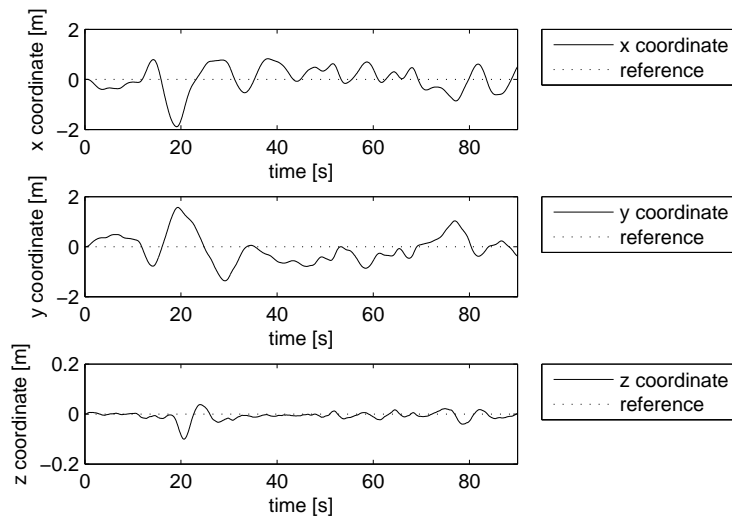


Figure 4.19: Position control using cascade PID

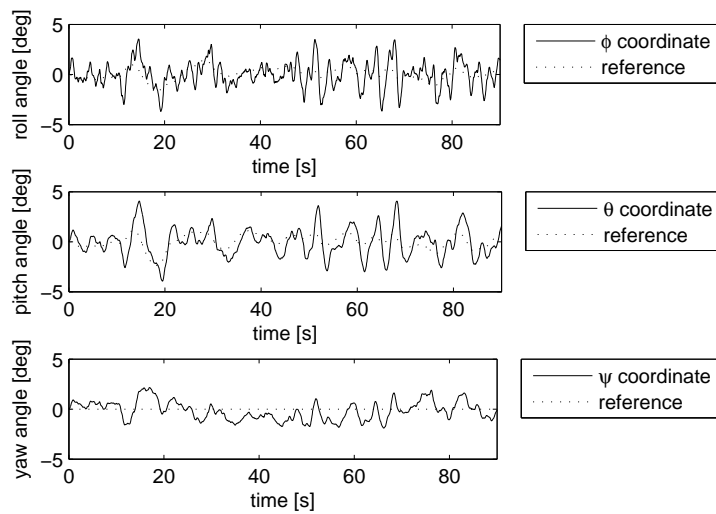


Figure 4.20: Attitude control using cascade PID

Although good attitude stabilization performance is achieved the position controllers have large position errors and weak disturbance rejection. The

degraded performance of the position control is probably due to the ignorance of nonlinear couplings between attitude and position states. Fig. 4.21 shows the forces created with cascade PID control. The control effort is similar to attitude stabilization alone.

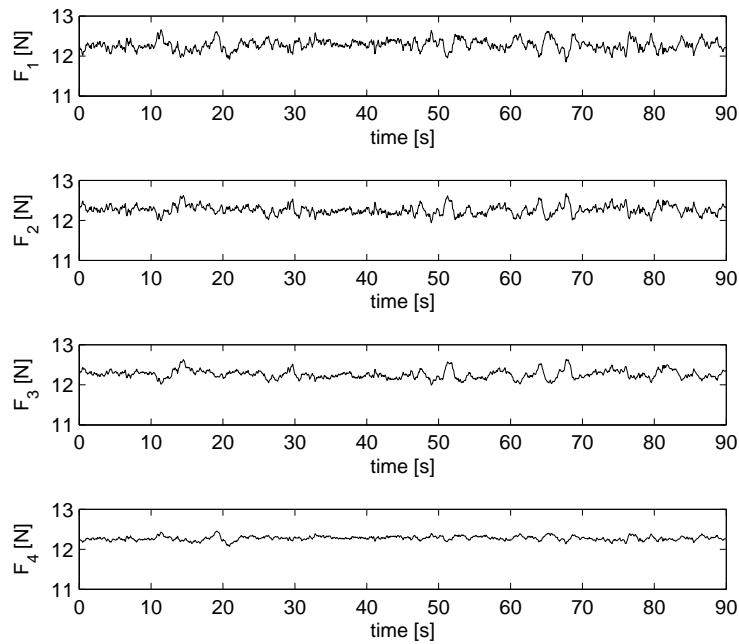


Figure 4.21: Forces created by rotors (Cascade PID)

LQR Controller Simulations

The performance of the LQR controller is evaluated on the nonlinear dynamic model of the vehicle given by (2) in MATLAB/Simulink. Q and R matrices used in LQR design are selected as

$$Q = 10^{-1} \cdot I_{12 \times 12}$$

$$R = \text{diag}(10^{-1}, 10, 10, 10)$$

With this selection of Q and R matrices the state variables have equal weight whereas the altitude control variable has less weight compared to roll, pitch and yaw state variables.

Starting with the initial configuration $P_w = (0, 0, 0)^T$ and $\alpha_w = (0, 0, 0)^T$ of the vehicle, the simulation results given in Fig. 4.22 and Fig. 4.23 show the variation of the position and attitude variables for the step reference inputs $P_{ref} = (5, -5, -10)^T$ and $\psi_r = -\pi/2$ under random disturbance.

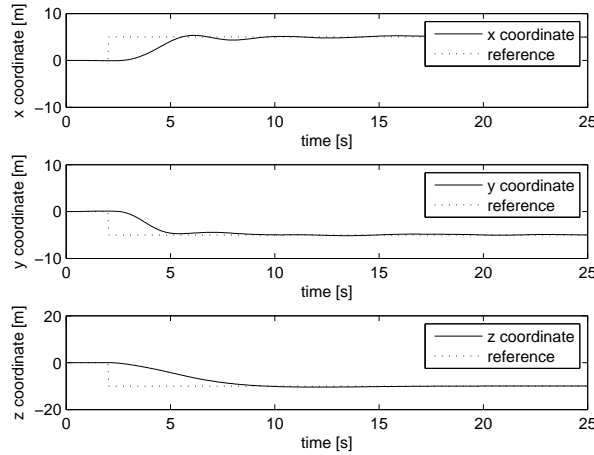


Figure 4.22: Position control using LQR

Note that position and angle references are tracked with small steady state errors. The lift forces generated by each rotor are shown in Fig. 4.24.

It is important to note that the control effort is small and the magnitude of the forces that need to be generated don't exceed the physical limits ($\simeq 16$ N) of the rotors and remain in the $\pm 20\%$ margin of the nominal thrust.

A second simulation is done for evaluating the trajectory tracking performance of the LQR controller. Again starting with the initial configuration

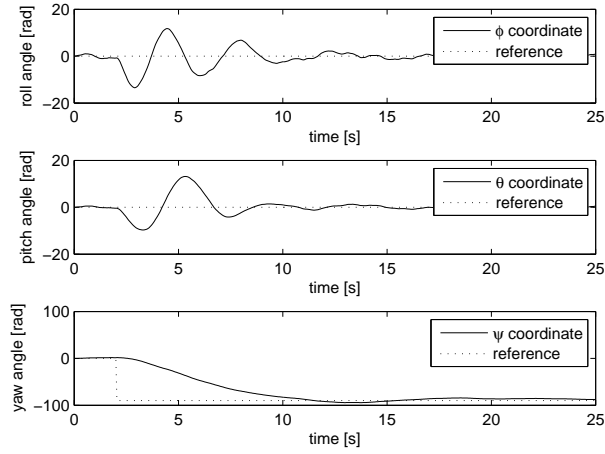


Figure 4.23: Attitude control using LQR

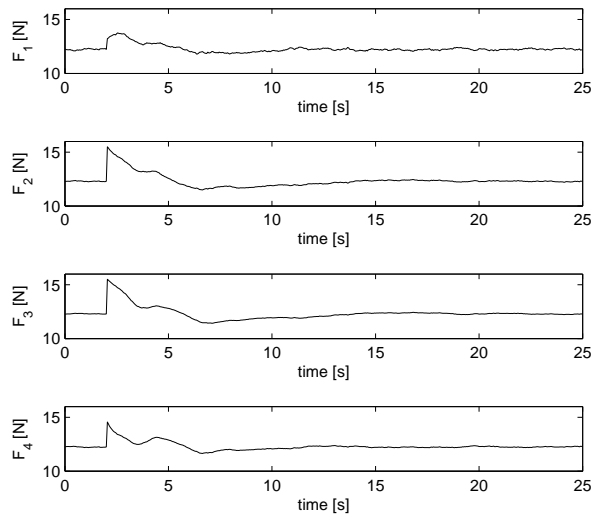


Figure 4.24: Forces created by rotors (LQR)

$P_w = (0, 0, 0)^T$ and $\alpha_w = (0, 0, 0)^T$ of the vehicle, the simulation results given in Fig. 4.26 and Fig. 4.27 show the variation of the position and attitude variables for the rectangular and helix trajectory given in Fig. 4.25.

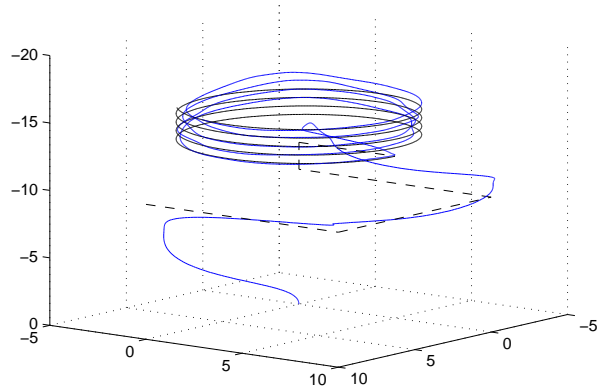


Figure 4.25: Rectangle and helix tracking

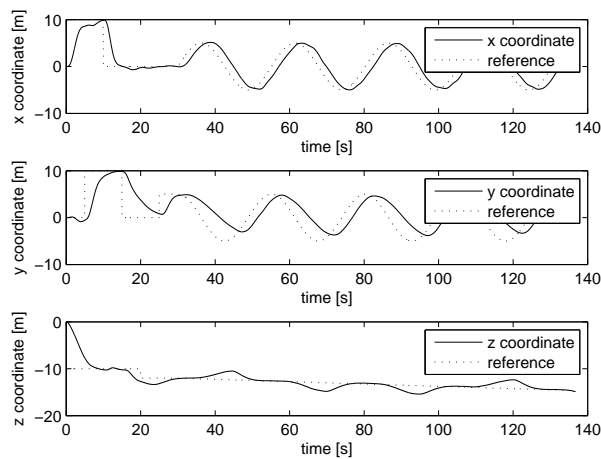


Figure 4.26: Rectangle and helix tracking using LQR (position)

The position references are tracked with a 3 sec. phase shift, but the trajectory points are followed and the path shape is preserved. The attitude stabilization plots (Fig. 4.27) show us that although the vehicle has deviated from the linear zone to nonlinear zone with roll and pitch angles of 20° , the system is stabilized and the trajectory is followed. The lift forces generated by each rotor are shown in Fig. 4.28. The physical limitations of the rotors

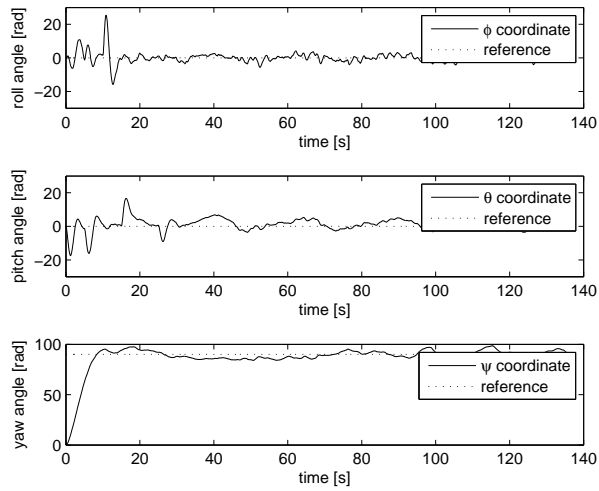


Figure 4.27: Rectangle and helix tracking using LQR (attitude)

are not exceeded.

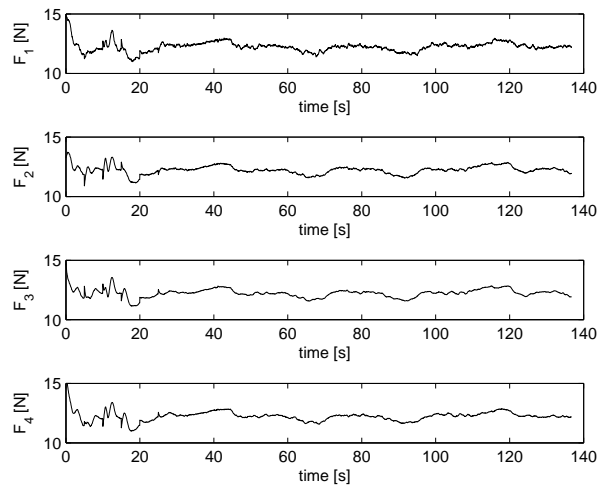


Figure 4.28: Rectangle and helix tracking using LQR (rotor forces)

Comparison of PID and LQR

The position control and attitude stabilization performances of cascade PID controller are given in Fig. 4.19, 4.20. Another simulation is done utilizing LQR controller under same reference and initial conditions. Fig. 4.29 and Fig. 4.30 show the position and attitude tracking performance of the LQR controller. Forces generated during the simulation are shown in Fig. 4.31. Comparison of two controllers performances is made by quantifying

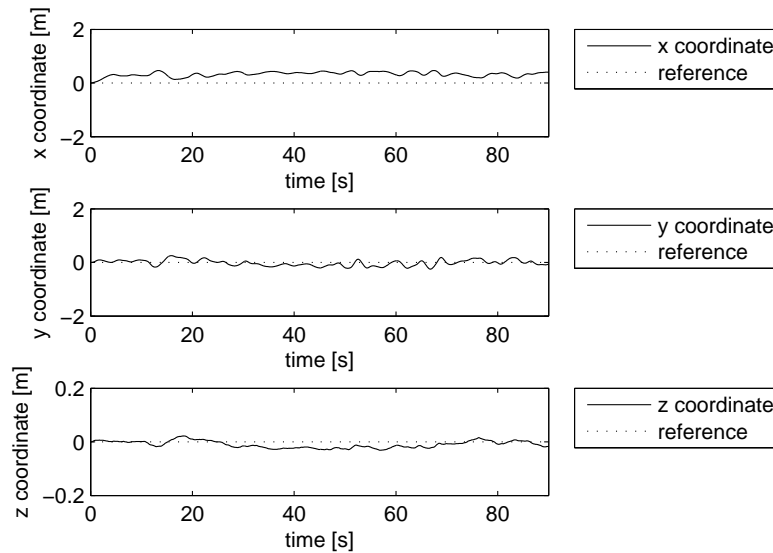


Figure 4.29: Position control (LQR)

the control effort and state tracking errors with RMS values. Table 4.1 shows the RMS values of force, position errors and attitude errors of two controllers. The RMS values of forces are calculated after extracting the nominal thrust values from measured thrust in order to quantify the control effort only. As seen from Table 4.1 LQR controller has better position tracking performance with less control effort. The attitude stabilization performance is also better

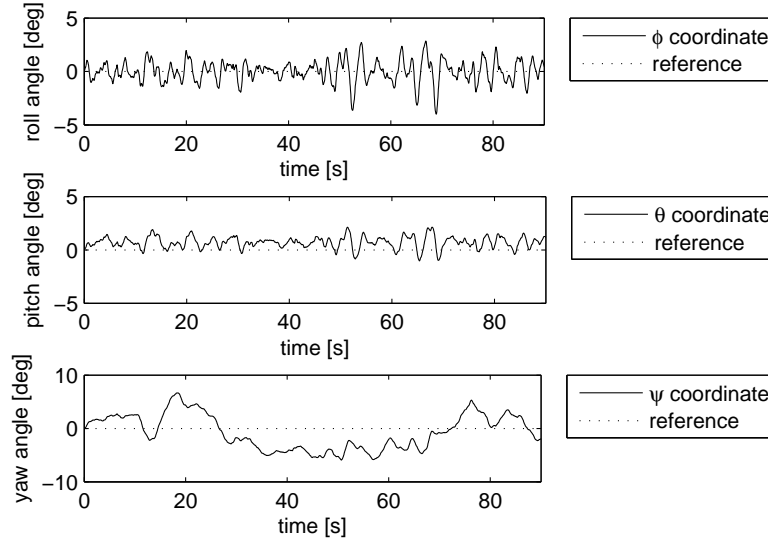


Figure 4.30: Attitude control (LQR)

Table 4.1: Position control & attitude stabilization performances

	Cascade PID	LQR
F_1	0.1366	0.0925
F_2	0.1168	0.0623
F_3	0.1099	0.0620
F_4	0.0582	0.0541
ϕ	1.3990	1.016
θ	1.5967	0.884
ψ	1.0246	3.447
x	0.6477	0.3358
y	0.6404	0.1155
z	0.0233	0.0162

than the cascade PID controller with a single weakness in yaw control. This is probably due to the large moment of inertia of the aerial vehicle around z axis. Performance of yaw tracking can be improved with further tuning

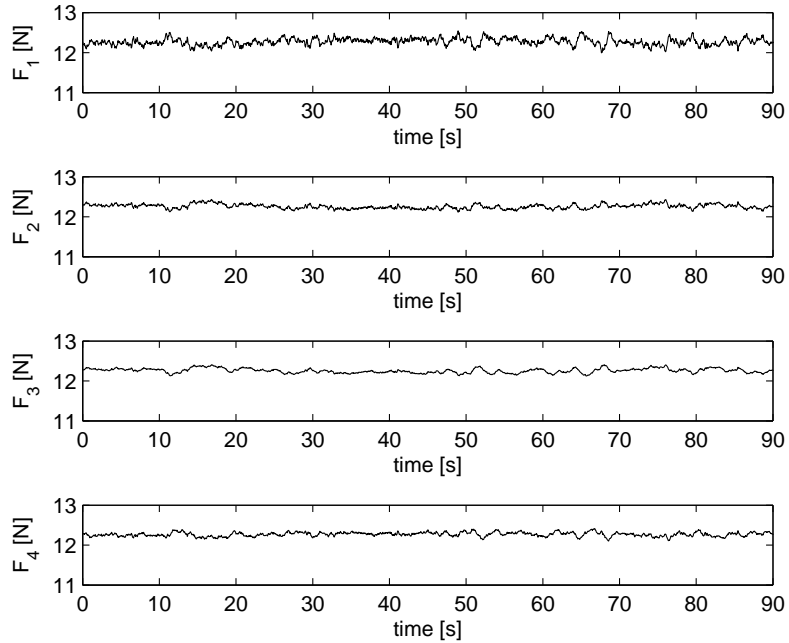


Figure 4.31: Forces created by rotors (LQR)

of weight matrices. As a result the LQR controller performs more optimally than cascade PID.

Transition Between Vertical and Horizontal Flight Modes

In this simulation, the transition from vertical to horizontal and back to vertical flight modes are commanded by joystick input. The proposed transition method between flight modes regulates the altitude of the vehicle in the presence of a tilt angle on the wings. Fig. 4.32 shows the change of tilt angles.

For this tilt angle commands the airstream magnitude and its angle during

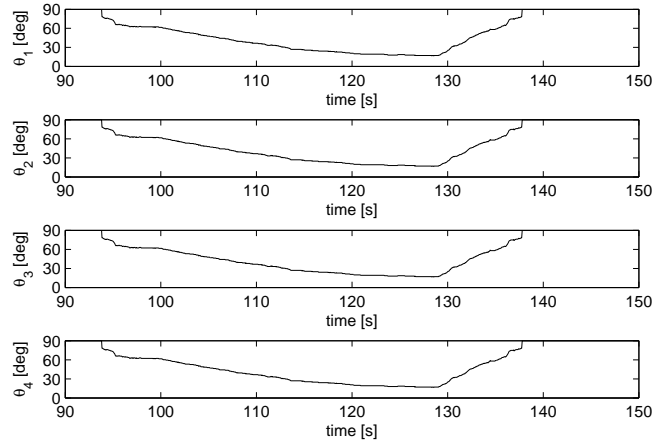


Figure 4.32: Change of tilt angles

transition are given in Fig. 4.33. The variation of effective angle of attack α_i

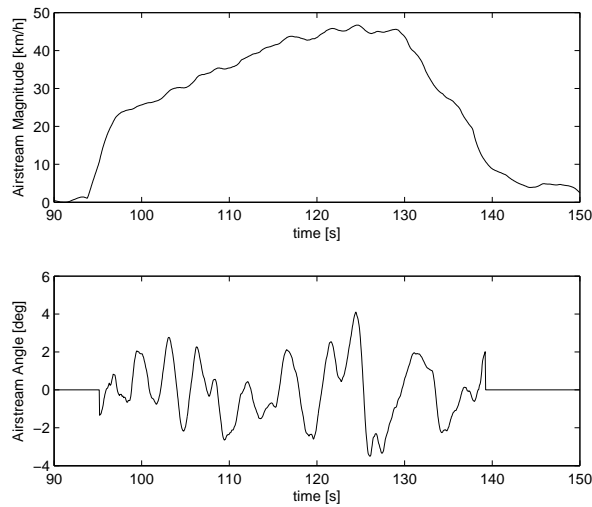


Figure 4.33: Airstream magnitude and its angle during transition

which depends on airstream angle and tilt angle θ_i are shown in Fig. 4.34.

The total lift and drag forces that appear on the body due to the wing

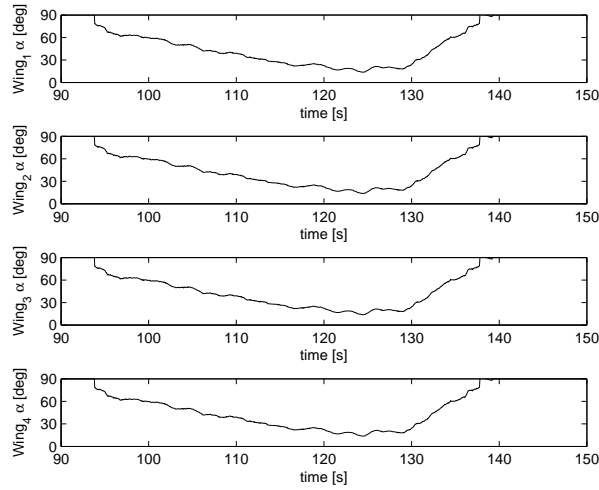


Figure 4.34: Effective angle of attack during transition

aerodynamics are given in Fig. 4.35.

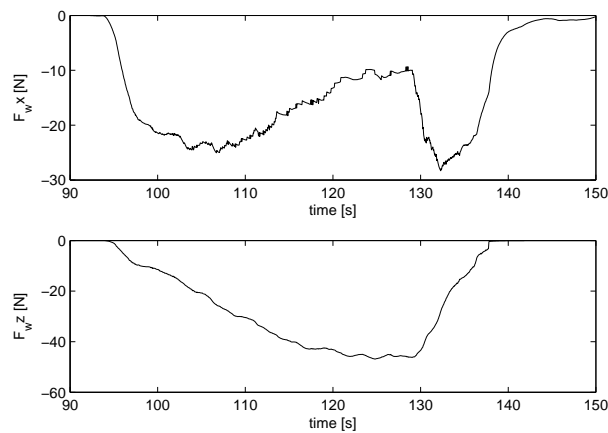


Figure 4.35: Lift and drag forces during transition

The thrust forces of actuators are given in Fig. 4.36.

As seen from Fig. 4.35 and Fig. 4.36 during transition from vertical to horizontal flight mode the lift force is transferred from actuators to the

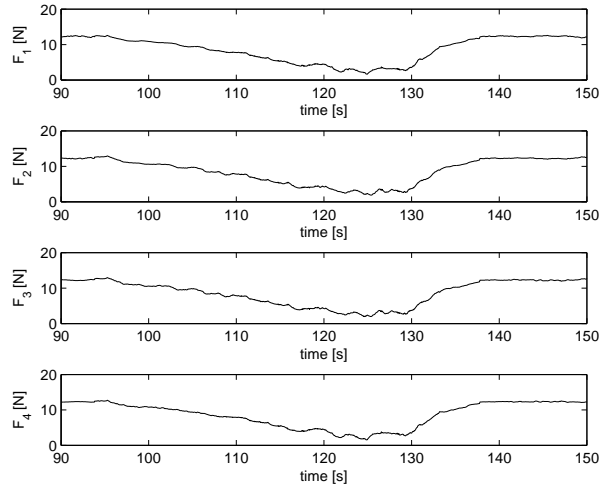


Figure 4.36: Rotor forces during transition

wings. The altitude regulation performance during this transition is given in Fig. 4.37.

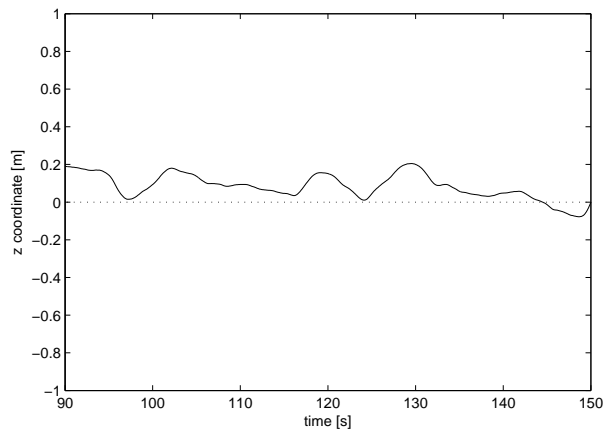


Figure 4.37: Altitude regulation during transition

As seen from Fig. 4.37 the altitude is maintained during transition processes between vertical and horizontal flight modes.

Chapter V

5 Experimental Results

Before starting with the experiments on the SUAVI prototype, the performance of the controllers are tested on a quadrotor platform that is very rigid. This quadrotor platform is built such that it mimics the actual prototype of SUAVI in VTOL mode. It has the same physical dimension, same weight of the actual prototype and a very close moment of inertias around roll and pitch axis.

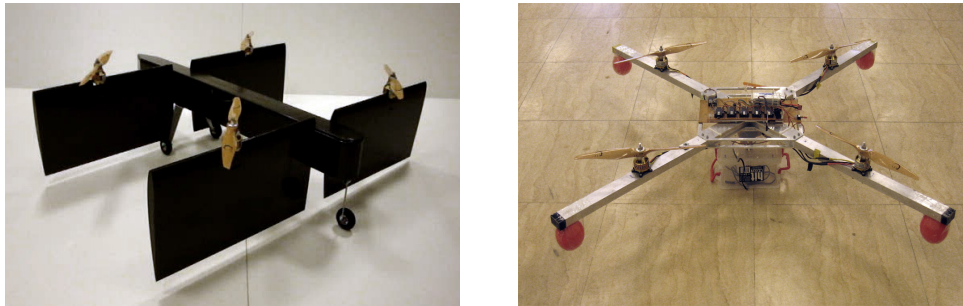


Figure 5.1: SUAVI prototype and the quadrotor test platform

5.1 Kalman Filter Experiments

The first experiments are done for verification of Kalman Filters implemented for roll and pitch angles. To start with a static angle of 50° is applied

for roll and pitch angles (Fig. 5.2, 5.3), and it is observed that the angles are converging to the actual values with a fast response. To verify the

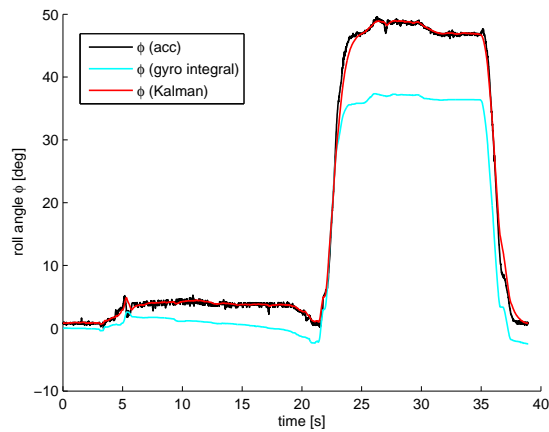


Figure 5.2: Roll estimation using Kalman filter (static)

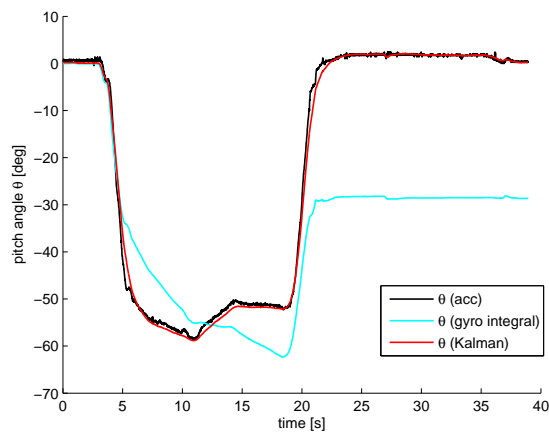


Figure 5.3: Pitch estimation using Kalman filter (static)

robustness of the algorithm the Kalman filters are tested again this time in dynamic environment (Fig. 5.4, 5.5). As seen from the plots the angle estimation from gyroscope integration is corrected over the trend line of the

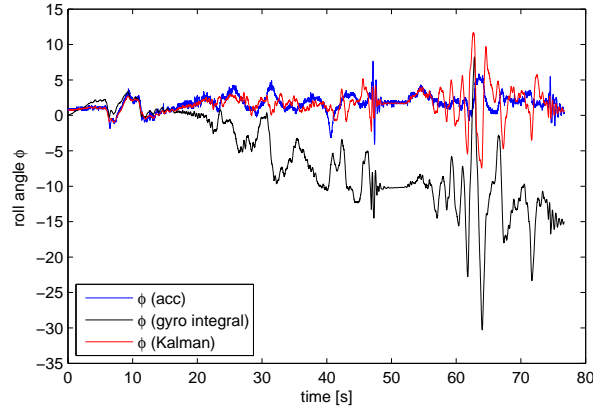


Figure 5.4: Roll estimation using Kalman filter (dynamic)

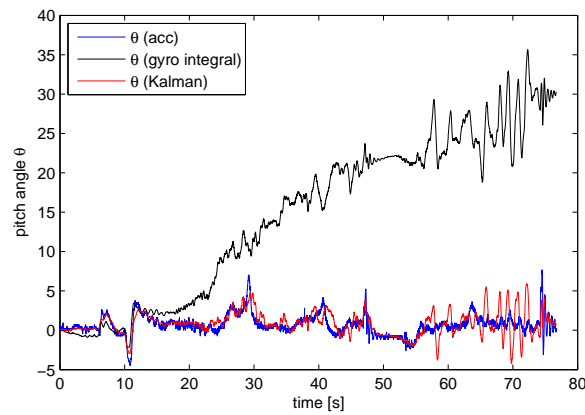


Figure 5.5: Pitch estimation using Kalman filter (dynamic)

accelerometer angle measurement, thus the drift is eliminated and the angle estimations can be used in control algorithms for vertical flight experiments.

5.2 Vertical Flight Experiments

The derived PID controller for attitude stabilization of SUAVI is implemented in onboard microprocessor of the vehicle. Because the drift of the yaw angle cannot be corrected without an external measurement, velocity

control is applied for the rotation around z-axis. The reference angles are generated via an R/C Transmitter from a user pilot with the aim of holding the vehicle stationary over a 3 m wide and 3 m long flight area. The tuning of PID parameters are done iteratively flight after flight. Fig. 5.6 shows the attitude stabilization performance of the aerial vehicle over a 15 sec. flight interval.

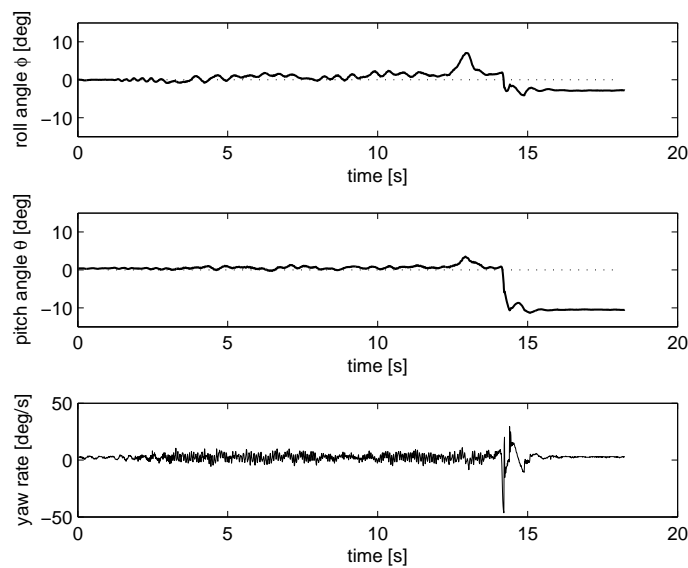


Figure 5.6: Attitude stabilization experiment using PID

As seen from Fig. 5.6, during the flight the roll and pitch angles remain around $\pm 3^\circ$ and hovering is achieved. The velocity control on the yaw axis works fine because there is no significant movement in yaw axis during hover flight. The measurements after 15 sec. show the inclination of the ground after landing. Several experiments are conducted to test the repeatability of performance. Fig. 5.7 shows the attitude stabilization data of a 20 sec. flight.

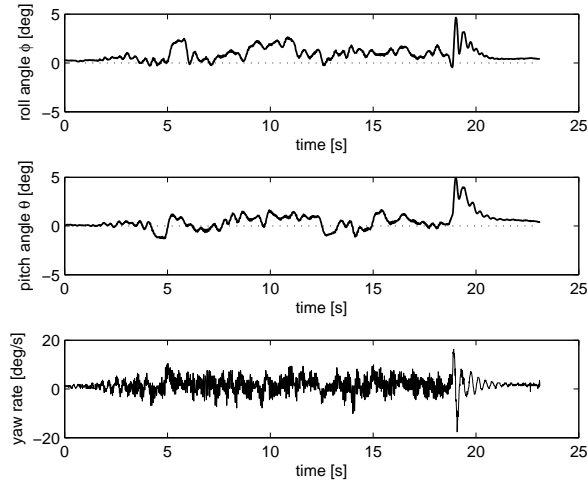


Figure 5.7: Attitude stabilization experiment using PID

Similar performance of the controller is observed in this flight. Having verified the repeatability a hovering experiment for longer time interval is performed. Fig. 5.8 shows another flight with a hovering duration of 50 sec.

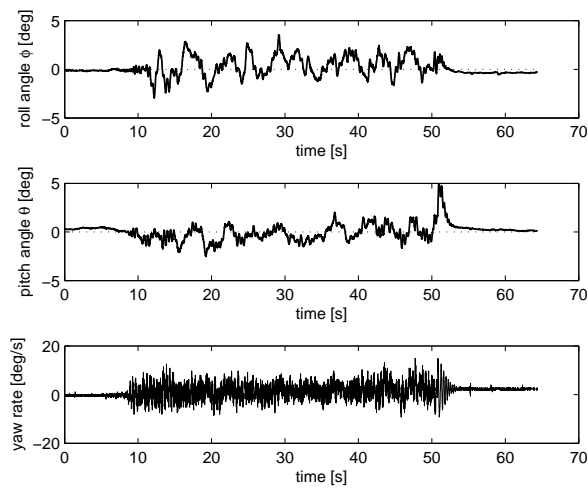


Figure 5.8: Attitude stabilization experiment using PID

From this flight it is observed that the attitude stabilization performance is not degrading over time and the roll and pitch stabilization is realized between angles $\pm 5^\circ$. Fig. 5.9 shows flight scenes from hovering experiment of SUAVI prototype.

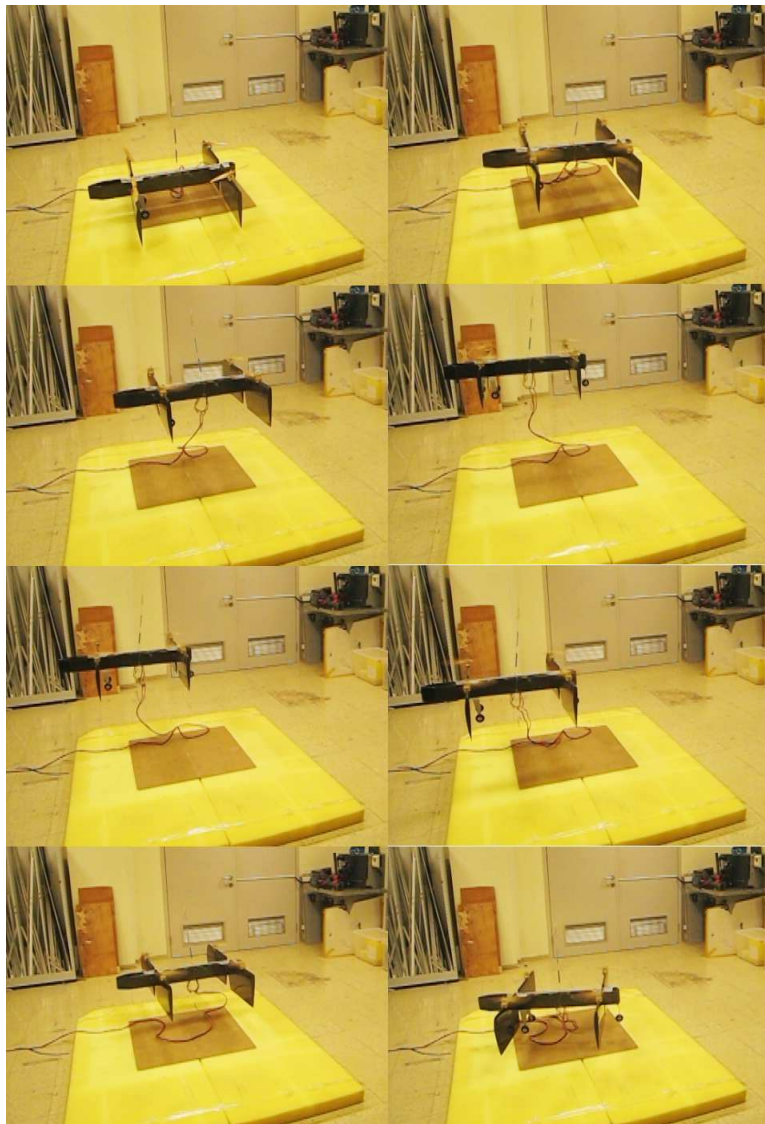


Figure 5.9: SUAVI vertical flight experiment

Chapter VI

6 Conclusion & Future Works

A new quadrotor Unmanned Aerial Vehicle with Tilt-Wing mechanism (SUAVI) with horizontal flight and vertical flight capabilities is presented in this thesis. The actuator and sensor integration of the vehicle is established and characterization of the sensor dynamics are made. Kalman filters are implemented and robust attitude estimation of the vehicle are obtained for control purposes.

The full mathematical model that incorporates the dynamics of horizontal flight, vertical flight (VTOL) and the transition mode is developed. Because the flight dynamics of the vehicle show very different characteristics in different flight modes, different control algorithms need to be implemented for each mode. Position control and attitude stabilization is done for VTOL mode and a method for transition from VTOL to horizontal flight mode is proposed. The performance of the controllers are investigated in simulation environment with 3D visualization and the results are promising. The LQR position controller is not implemented on the vehicle because the full state information is not available with the existing sensory data, but PID controller's performance for attitude stabilization are verified with VTOL flight experiments.

Future works include incorporation of sonar sensors, higher resolution

magnetometers, GPS units and pitot tubes for state estimations and design of flight controllers for horizontal flight mode and the transition mode of SUAVI.

References

- [1] M. A. Turk, D. G. Morgenthaler, K. D. Gremban, and M. Marra. VITS—a Vision System for Autonomous Land Vehicle Navigation. *Pattern Analysis and Machine Intelligence, IEEE Transactions on*, 10(3):342–361, May 1988.
- [2] ASD Reports. *The Unmanned Aerial Vehicles (UAV) Market 2009-2019*. Visiongain, May 2009.
- [3] JAPCC Flight Plan for Unmanned Aircraft Systems in NATO (2008 edition), July 2009. [online] http://japcc.de/fileadmin/user_upload/projects/nato_flight_plan_for_uas/Flightplan_2008/UAV_Flight_Plan_-_Update_2008.zip.
- [4] Unmanned Aircraft Systems, July 2009. [online] http://www.uvs-info.com/Yearbook2007/189_REF_Civil-UAS.pdf.
- [5] J. M. McMichael and M. S. Francis. Micro Air Vehicles - Toward a New Dimension in Flight. *Defense Advanced Research Projects Agency*, August 1997.
- [6] J. Escareo, A. Sanchez, O. Garcia, and R. Lozano. Triple Tilting Rotor Mini-UAV: Modeling and Embedded Control of the Attitude. In *American Control Conference, 2008*, pages 3476–3481, June 2008.
- [7] W.E. Green and P.Y. Oh. Autonomous Hovering of a Fixed-Wing Micro Air Vehicle. In *Robotics and Automation, 2006. ICRA 2006. Proceedings 2006 IEEE International Conference on*, pages 2164–2169, May 2006.

- [8] J. M. Grasmeyer and M. T. Keennon. Development of the Black Widow Micro Air Vehicle. *39th AIAA Aerospace Sciences Meeting and Exhibit*, 2001.
- [9] Delfly Micro, July 2009. [online] <http://www.delfly.nl/?site=DIII&menu=info&lang=en>.
- [10] K. S. Shigeoka. Velocity and Altitude Control of an Ornithopter Micro Aerial Vehicle. Master's thesis, University of Utah, 2007.
- [11] Jean-Christophe Zufferey, Alexis Guanella, Antoine Beyeler, and Dario Floreano. Flying over the Reality Gap: From Simulated to Real Indoor Airships. *Autonomous Robots*, 21(3):243–254, 2006.
- [12] F. Kendoul, I. Fantoni, and R. Lozano. Modeling and Control of a Small Autonomous Aircraft Having Two Tilting Rotors. *Robotics, IEEE Transactions on*, 22(6):1297–1302, December 2006.
- [13] Draganflyer X6 Helicopter Tech Specs, July 2009. [online] <http://www.draganfly.com/uav-helicopter/draganflyer-x6/specifications/>.
- [14] T-Hawk MAV, July 2009. [online] <http://www.missionready.com/pdf/thawkmavbrochure.pdf>.
- [15] J. Wilds. Real Options In a Micro Air Vehicle System. *ESD.71 Application Portfolio*, 2006.
- [16] M. Harries. Rise of the Machines. *BBC Focus Magazine*, pages 22–28, June 2009.

- [17] Raven RQ-11B, July 2009. [online] http://www.avinc.com/downloads/AV_RAVEN-INT_V10109.pdf.
- [18] Desert Hawk III Putting Capability in the Hands of the Warfighter, July 2009. [online] <http://www.lockheedmartin.com/data/assets/14502.pdf>.
- [19] Orbiter, July 2009. [online] http://www.aaicorp.com/pdfs/aai_smaluavfamily_04-29-09.pdf.
- [20] Malazgirt, July 2009. [online] <http://www.baykarmakina.com/heliuav>.
- [21] QTW-UAS FS4, July 2009. [online] http://www.ghcraft.com/QTW/pdf/081001_QTW_FS4e.pdf.
- [22] DraganFly Tango, July 2009. [online] <http://www.draganfly.com/uav-airplane/tango/specifications/>.
- [23] The BLIMP 2 C, July 2009. [online] <http://www.surveycopter.fr/english/uavs-blimp/blimp-2-c.html>.
- [24] J. V. Hogge. Development of a Miniature VTOL Tail-Sitter Unmanned aerial Vehicle. Master's thesis, Brigham Young University, 2008.
- [25] Yamaha Autonomous-flight Unmanned Helicopter, July 2009. [online] <http://www.yamaha-motor.co.jp/global/news/2002/02/06/sky.html>.
- [26] MQ-8B Fire Scout Vertical Unmanned Aircraft System, July 2009. [online] http://www.as.northropgrumman.com/products/mq8bfirescout_navy/assets/fs-fact-sheet.pdf.

- [27] Eagle Eye Pocket Guide, July 2009. [online] http://www.bellhelicopter.com/en/aircraft/military/pdf/EagleEye_PG_05_web.pdf.
- [28] Predator/MQ-1 Predator Persistent ISR and Strike, July 2009. [online] http://www.ga-asi.com/products/aircraft/pdf/MQ-1_Predator.pdf.
- [29] RQ-4 Global Hawk High-Altitude, Long-Endurance Unmanned Aerial Reconnaissance System, July 2009. [online] http://www.as.northropgrumman.com/products/ghrq4b/assets/HALE_Factsheet.pdf.
- [30] Investigation of the Helios Prototype Aircraft - Mishap Volume I Mishap Report, July 2009. [online] http://www.nasa.gov/pdf/64317main_helios.pdf.
- [31] S. Bouabdallah. *Design and Control of Quadrotors with Application to Autonomous Flight*. PhD thesis, Ecole Polytechnique Federale de Lausanne, 2007.
- [32] V/STOL: The First Half-Century, Same Propulsion System for Hover and Forward Flight, July 2009. [online] <http://www.aiaa.org/tc/vstol/same.html>.
- [33] Tilt-rotor and tilt-wing aircraft, July 2009. [online] http://www.aviastar.org/helicopters_eng/tiltrotor.html.
- [34] U.S. Department of Transportation. *Flight Training Handbook*. Aviation Book Co; Rev Sub edition, May 1980.

- [35] K. T. Öner, E. Çetinsoy, M. Ünel, M. F. Akşit, İ. Kandemir, and K. Gülez. Yeni Bir İnsansız Hava Aracının (SUAVİ) Mekanik ve Aerodinamik Tasarımı. In *TOK'08: Otomatik Kontrol Ulusal Toplantısı, İstanbul Teknik Üniversitesi*, volume 36, November 2008.
- [36] Rimfire Outrunner Brushless Motors 42 mm diameter / 40 mm length, July 2009. [online] <http://www.electrifly.com/motors/motors-rimfire-42-40.html>.
- [37] Silver Series Brushless Electronic Speed Controls, July 2009. [online] http://manuals.hobbico.com/gpm/gpmm1800-manual-v1_1.pdf.
- [38] IMU 6 Degrees of Freedom v4 Data Sheet, July 2009. [online] <http://www.sparkfun.com/datasheets/Sensors/DataSheet-6DOF-v4-Rev1.pdf>.
- [39] K. T. Öner, E. Çetinsoy, E. Sırımoğlu, T. Ayken, C. Hançer, M. Ünel, M. F. Akşit, İ. Kandemir, and K. Gülez. Yeni Bir İnsansız Hava Aracının (SUAVİ) Prototip Üretimi ve Algılayıcı Eyleyici Entegrasyonu. In *TOK'09: Otomatik Kontrol Ulusal Toplantısı, Yıldız Teknik Üniversitesi*, 2009.
- [40] M. J. Abzug and E. E. Larrabee. *Airplane Stability and Control Second Edition*. Cambridge University Press, 2002.
- [41] M.Y. Amir and V. Abbass. Modeling of Quadrotor Helicopter Dynamics. In *Smart Manufacturing Application, 2008. ICSMA 2008. International Conference on*, pages 100–105, April 2008.
- [42] P. McKerrow. Modelling the Draganflyer four-rotor helicopter. In *Robotics and Automation, 2004. Proceedings. ICRA '04. 2004 IEEE In-*

- ternational Conference on*, volume 4, pages 3596–3601 Vol.4, 26-May 1, 2004.
- [43] K. Kondak, M. Bernard, N. Meyer, and G. Hommel. Autonomously Flying VTOL-Robots: Modeling and Control. In *Robotics and Automation, 2007 IEEE International Conference on*, pages 736–741, April 2007.
- [44] G. M. Hoffmann, H. Huang, S. L. Wasl, and C. J. Tomlin. Quadrotor helicopter flight dynamics and control:theory and experiment. In *In Proc. of the AIAA Guidance, Navigation, and Control Conference*, August 2007.
- [45] P. B. Harendra, M. J. Joglekar, T. M. Gaffey, and R. L. Marr. A Mathematical Model for Real-Time Flight Simulation of the Bell Model 301 Tilt Rotor Research Aircraft, 1973. [online] http://ntrs.nasa.gov/archive/nasa/casi.ntrs.nasa.gov/19730022217_1973022217.pdf.
- [46] A. Okan, O. Tekinalp, Kavsaoglu M. Ş., Ö. Armutçuoğlu, and E. Tulunay. Flight Mechanics Analysis of a Tilt Rotor UAV. *Atmospheric Flight Mechanics Conference and Exhibit 1999 AIAA*, August 1999.
- [47] J.J. Dickeson, D. Miles, O. Cifdaloz, V.L. Wells, and A.A. Rodriguez. Robust LPV H Gain-Scheduled Hover-to-Cruise Conversion for a Tilt-Wing Rotorcraft in the Presence of CG Variations. In *American Control Conference, 2007. ACC '07*, pages 5266–5271, July 2007.
- [48] Suzuki, S. and Zhijia, R. and Horita, Y. and Nonami,K. and Kimura, G. and Bando, T. and Hirabayashi, D. and Furuya, M. and Yasuda, K. Attitude Control of Quad Rotors QTW-UAV with Tilt Wing Mecha-

- nism. *Transactions of the Japan Society of Mechanical Engineers. C*, 73(731):2012–2019, July 2007.
- [49] K. T. Öner, E. Çetinsoy, M. Ünel, İ. Kandemir, M. F. Akşit, and K. Gülez. Yeni Bir İnsansız Hava Aracının (SUAVİ) Dikey Uçuş Kipi İçin Dinamik Modeli ve Yörünge Kontrolü. In *TOK'08: Otomatik Kontrol Ulusal Toplantısı, İstanbul Teknik Üniversitesi*, November 2008.
- [50] K. T. Öner, E. Çetinsoy, M. Ünel, M. F. Akşit, İ. Kandemir, and K. Gülez. Modeling and Position Control of a New Quad-rotor Unmanned Aerial Vehicle with Tilt-Wing Mechanism. In *Proceedings of World Academy of Science, Engineering and Technology. ICCARV'08 International Conference on Control, Automation, Robotics and Vision*, volume 36, September 2008.
- [51] T. Madani and A. Benallegue. Backstepping Control for a Quadrotor Helicopter. In *Intelligent Robots and Systems, 2006 IEEE/RSJ International Conference on*, pages 3255–3260, Oct. 2006.
- [52] I. H. Abbott and A. E. von. Doenhoff. *Theory of Wing Sections*. Dover Publications Inc., 1959.
- [53] R. E. Sheldahl and P. C. Klimas. Aerodynamic Characteristics of Seven Symmetrical Airfoil Sections Through 180 Degree Angle of Attack For Use in Aerodynamic Analysis of Vertical Axis Wind Turbines. July 1981. [online] <http://prod.sandia.gov/techlib/access-control.cgi/1980/802114.pdf>.
- [54] S. Bouabdallah, A. Noth, and R. Siegwart. Pid vs lq control techniques applied to an indoor micro quadrotor. In *Intelligent Robots and Sys-*

- tems, 2004. (IROS 2004). Proceedings. 2004 IEEE/RSJ International Conference on*, volume 3, pages 2451–2456 vol.3, Sept.-2 Oct. 2004.
- [55] T Bresciani. Modeling Identification and Control of a Quadrotor Helicopter. Master’s thesis, Department of Automatic Control, Lund University, 2008.
- [56] B. Erginer and E. Altug. Modeling and PD Control of a Quadrotor VTOL Vehicle. In *Intelligent Vehicles Symposium, 2007 IEEE*, pages 894–899, June 2007.
- [57] A. Tayebi and S. McGilvray. Attitude Stabilization of a Four-rotor Aerial Robot. In *Decision and Control, 2004. CDC. 43rd IEEE Conference on*, volume 2, pages 1216–1221 Vol.2, Dec. 2004.
- [58] I. D. Cowling, O. A. Yakimenko, and A. K. Whidborne, J. F. and Cooke. A Prototype of an Autonomous Controller for a Quadrotor UAV. July 2007.
- [59] Holger Voos. Nonlinear State-dependent Riccati Equation Control of a Quadrotor UAV. In *Computer Aided Control System Design, 2006 IEEE International Conference on Control Applications, 2006 IEEE International Symposium on Intelligent Control, 2006 IEEE*, pages 2547–2552, Oct. 2006.
- [60] M.G. Earl and R. D’Andrea. Real-time Attitude Estimation Techniques Applied to a Four Rotor Helicopter. In *Decision and Control, 2004. CDC. 43rd IEEE Conference on*, volume 4, pages 3956–3961 Vol.4, Dec. 2004.

- [61] DongBin Lee, T.C. Burg, Bin Xian, and D.M. Dawson. Output Feedback Tracking Control of an Underactuated Quad-Rotor UAV. In *American Control Conference, 2007. ACC '07*, pages 1775–1780, July 2007.
- [62] T. Madani and A. Benallegue. Backstepping control with exact 2-sliding mode estimation for a quadrotor unmanned aerial vehicle. In *Intelligent Robots and Systems, 2007. IROS 2007. IEEE/RSJ International Conference on*, pages 141–146, 29 2007-Nov. 2 2007.
- [63] S. L. Waslander, G. M. Hoffmann, J. S. Jang, and C. J. Tomlin. Multi-agent quadrotor testbed control design: Integral sliding mode vs reinforcement learning. In *In Proceedings of the IEEE/RSJ International Conference on Intelligent Robotics and Systems 2005*, pages 468–473, 2005.
- [64] A. Hably and N. Marchand. Global Stabilization of a Four Rotor Helicopter with Bounded Inputs. In *Intelligent Robots and Systems, 2007. IROS 2007. IEEE/RSJ International Conference on*, pages 129–134, 29 2007-Nov. 2 2007.
- [65] S. Bouabdallah and R. Siegwart. Full Control of a Quadrotor. In *Intelligent Robots and Systems, 2007. IROS 2007. IEEE/RSJ International Conference on*, pages 153–158, 29 2007-Nov. 2 2007.
- [66] L. Beji, A. Abichou, and K.M. Zemalache. Smooth control of an x4 bidirectional rotors flying robot. In *Robot Motion and Control, 2005. RoMoCo '05. Proceedings of the Fifth International Workshop on*, pages 181–186, June 2005.

- [67] N. Guenard, T. Hamel, and V. Moreau. Dynamic modeling and intuitive control strategy for an "X4-flyer". In *Control and Automation, 2005. ICCA '05. International Conference on*, volume 1, pages 141–146 Vol. 1, June 2005.
- [68] T. Hamel, R. Mahony, R. Lozano, and J. Ostrowski. Dynamic Modeling and Configuration Stabilization for an X4-Flyer. In *Proc. of the 15th Triennial World Congress of IFAC*, 2002.
- [69] K. T. Öner, E. Çetinsoy, E. Sırımoğlu, T. Ayken, M. Ünel, M. F. Akşit, İ. Kandemir, and K. Gülez. Döner Kanat Mekanizmasına Sahip Yeni Bir İnsansız Hava Aracının (SUAVİ) Modellenmesi ve Kontrolü. In *TOK'09: Otomatik Kontrol Ulusal Toplantısı, Yıldız Teknik Üniversitesi*, 2009.
- [70] J. A. Rios and E. White. Fusion Filter Algorithm Enhancements For a MEMS GPS/IMU. *Proceedings of the 14th International Technical Meeting of the Satellite Division of the Institute of Navigation ION GPS 2001*, pages 1382 – 1393, September 2001.
- [71] W. Yongliang, W. Tianmiao, L. Jianhong, W. Chaolei, and Z. Chen. Attitude Estimation for Small Helicopter Using Extended Kalman Filter. In *Robotics, Automation and Mechatronics, 2008 IEEE Conference on*, pages 577–581, Sept. 2008.
- [72] R. V. D. Merwe and E. Wan. Sigma-Point Kalman Filters For Integrated Navigation. *Proceedings of the 60th Annual Meeting ION*, 2004.
- [73] J.M. Roberts, P.I. Corke, and G. Buskey. Low-cost Flight Control System for a Small Autonomous Helicopter. In *Robotics and Automation*,

2003. *Proceedings. ICRA '03. IEEE International Conference on*, volume 1, pages 546–551 vol.1, Sept. 2003.
- [74] M. Euston, P. Coote, R. Mahony, Jonghyuk Kim, and T. Hamel. A complementary filter for attitude estimation of a fixed wing uav. In *Intelligent Robots and Systems, 2008. IROS 2008. IEEE RSJ International Conference on*, pages 340–345, September 2008.
- [75] Young Soo Suh. Attitude Estimation Using Low Cost Accelerometer and Gyroscope. In *Science and Technology, 2003. Proceedings KORUS 2003. The 7th Korea-Russia International Symposium on*, volume 2, pages 423–427 vol.2, June-6 July 2003.
- [76] Measurement of a Vehicle’s Dynamic Motion, 2005. [online] http://www.xbow.com/support/support_pdf_files/imuappnote.pdf.
- [77] Integrated Dual-Axis Gyro IDG-300, July 2009. [online] http://www.invensense.com/shared/pdf/DS_IDG300.pdf.
- [78] R. E. Kalman. A New Approach to Linear Filtering and Prediction Problems. *Transactions of the ASME, Journal of Basic Engineering*, (82 (Series D)):35–45, 1960.
- [79] 1.5g-6g Three Axis Low-g Micromachined Accelerometer, July 2009. [online] http://www.freescale.com/files/sensors/doc/data_sheet/MMA7260QT.pdf.
- [80] 1, 2 and 3 Axis Magnetic Sensors HMC1051/HMC1052/HMC1053, July 2009. [online] <http://www.ssec.honeywell.com/magnetic/datasheets/HMC105X.pdf>.

[81] Magnetic Field Calculator, July 2009. [online] <http://www.ngdc.noaa.gov/geomagmodels/IGRFWMM.jsp>.